日本磁気学会
ISSN 2432-0250
Journal of the Magnetics Society of Japan
Electronic Journal URL: https://www.jstage.jst.go.jp/browse/msjmag

Vol.46 No.2　2022

Journal

JOURNAL OF THE MAGNETICS SOCIETY OF JAPAN

Vol.46 No.2 2022

日本磁気学会

ISSN 2432-0250

HP: http://www.magnetics.jp/ e-mail: msj@bj.wakwak.com

Electronic Journal: http://www.jstage.jst.go.jp/browse/msjmag

Journal of the Magnetics Society of Japan
Vol. 46, No. 2

Electronic Journal URL: https://www.jstage.jst.go.jp/browse/msjmag

CONTENTS

J. Magn. Soc. Jpn., **46**, 22-36 (2022)

<Review>

Hysteresis Modeling for Power Magnetic Devices Based on Magnetic Circuit Method

Y. Hane

Graduate School of Engineering, Tohoku Univ., *6-6-11 Aoba Aramaki, Aoba-ku, Sendai 980-8579, Japan*

This paper introduces the latest research achievements on the hysteresis modeling for power magnetic devices based on the magnetic circuit method. First, the magnetic circuit model considering the magnetic hysteresis behavior is derived. Next, this magnetic circuit model is developed to the reluctance network model, to analyze more complicated devices such as an electric motor. Furthermore, this magnetic circuit model is improved to take the dynamic hysteresis characteristics including the skin effect into account. Finally, the prediction method of the deteriorated hysteresis loops in core material due to machining process is established.

Key words: magnetic circuit method, Landau-Lifshitz-Gilbert (LLG) equation, play model, reluctance network analysis (RNA), Cauer circuit

1. Introduction

In recent years, quantitative analysis of the iron loss taking the magnetic hysteresis behavior into account is essential to the development of high-efficiency electric machines. In many cases of machine design and analysis based on numerical analysis using the finite element method (FEM), the iron loss is generally calculated by using approximate formulas, such as the Steinmetz' equation, in the post-processing of a main electromagnetic field analysis [1)-5)]. However, their calculation accuracies are insufficient when the exciting voltage waveform is significantly distorted. To improve the calculation accuracy, the parameters in the formulas must be identified for each waveform, which is a huge practical drawback. Thus, various kinds of high-accuracy hysteresis models have been presented so far [6)-8)]. However, most of the general-purpose FEM programs neglect the magnetic hysteresis since it generally takes a lot of calculation time and computer memory. Therefore, it is strongly required to establish a simple and practical iron loss calculation method considering the magnetic hysteresis.

To solve the above problem, the magnetic circuit method is one of the practical solutions because an analytical model is very simple, the calculation accuracy is relatively high, and it is easy to combine with an electric circuit and a motion equation. Therefore, this paper introduces the latest research achievements on the hysteresis modeling for electric machines based on the magnetic circuit. The Chapter 2 describes the magnetic circuit model considering the magnetic hysteresis behavior. The Chapter 3 describes that this magnetic circuit model is developed to the reluctance network model, to analyze more complicated devices such as an electric motor. The Chapter 4 describes that the magnetic circuit model, presented in the Chapter 2, is improved to take the dynamic hysteresis characteristics including the skin effect into account. The Chapter 5 describes the prediction method of the deteriorated hysteresis loops in core material due to machining process.

Corresponding author: Y. Hane (e-mail: yoshiki.hane.e2@tohoku.ac.jp).

2. Magnetic Circuit Model Considering Magnetic Hysteresis Behavior by Incorporating Play Model

In this Chapter, the magnetic circuit model considering the magnetic hysteresis behavior by incorporating the play model [9), 10)], and the derivation method of the play model by using the simplified Landau-Lifshitz-Gilbert (LLG) equation [11)-13)], which are the bases of the analyses in the following chapters, are described.

2.1 Basis of magnetic circuit method

Fig. 1(a) illustrates a ring core with a winding of N turns. A cross section, magnetic path length, and permeability of a core are S_i, l_i, and μ, respectively. When current i flows in the winding, a relationship between magnetomotive force (MMF) Ni and flux ϕ can be expressed in the following equation [14)]:

$$Ni = R_m \phi, \text{where } R_m = \frac{l_i}{\mu S_i}. \quad (1)$$

In Eq. (1), letting Ni and ϕ correspond to voltage v and current i in an electric circuit, it is understood that the same relationship as the Ohm's low exists between Ni and ϕ. Accordingly, a ring core in Fig. 1(a) can be expressed in the form of a magnetic circuit shown in Fig. 1(b). In this figure, R_m, which corresponds to a resistance in an electric circuit, is called "reluctance".

As mentioned above, there is a high degree of similarity between magnetic and electric circuits. However, actual magnetic material has the magnetic nonlinearity due to the magnetic saturation and hysteresis and causes the iron loss due to the magnetic hysteresis and eddy current. Therefore, it is necessary to derive the magnetic circuit model taking these complicated magnetic phenomena into consideration, to

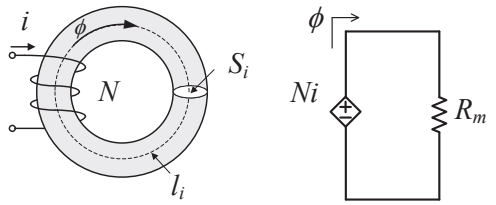

(a) Ring core. (b) Magnetic circuit.

Fig. 1 Ring core and its magnetic circuit.

obtain more accurate calculation result.

2.2 Derivation of magnetic circuit model considering magnetic hysteresis behavior

The iron loss of soft ferromagnetic material W_i can be approximately calculated as the sum of hysteresis loss, classical eddy current loss, and anomalous eddy current loss, by using the following Bertotti's equation [2].

$$W = A_h f B_m^{\ 2} + A_e f^2 B_m^{\ 2} + A_a f^{1.5} B_m^{\ 1.5}, \tag{2}$$

where a frequency is f, maximum magnetic flux density is B_m, and coefficients are A_h, A_e, and A_a, respectively. Here, Fig. 2 shows a schematic diagram of the hysteresis loop under ac excitation. The magnetic field H at the operating point c in this figure can be represented by the sum of the component between a and b determined by the dc hysteresis and the component between b and c which changes depending on the time derivative of the magnetic flux density B. Therefore, a relationship between H and B can be obtained as follows:

$$H = \begin{cases} H_{dc} + \gamma_1 \dfrac{dB}{dt} + \gamma_2 \left|\dfrac{dB}{dt}\right|^{0.5} & \left(\dfrac{dB}{dt} > 0\right) \\ H_{dc} + \gamma_1 \dfrac{dB}{dt} - \gamma_2 \left|\dfrac{dB}{dt}\right|^{0.5} & \left(\dfrac{dB}{dt} < 0\right) \end{cases}, \tag{3}$$

where the dc field is H_{dc}, and coefficients are γ_1 and γ_2, respectively. In Eq. (3), each of the first, second, and third terms represents the dc hysteresis, classical eddy current loss, and anomalous eddy current loss, respectively. This equation can be transformed into a relationship between Ni and ϕ as follows:

$$Ni = H_{dc} l_i + \frac{\gamma_1 l_i}{S_i} \frac{d\phi}{dt} \pm \frac{\gamma_2 l_i}{S_i^{0.5}} \left|\frac{d\phi}{dt}\right|^{0.5}. \tag{4}$$

Eq. (4) can be expressed as the magnetic circuit model shown in Fig. 3. In this model, several kinds of representation methods of the dc hysteresis have been proposed, such as the look-up-table [15], simplified LLG equation [11)-13)], and play model [9), 10)], while the classical and anomalous eddy current losses are simply denoted by the inductance element and dependent source of flux, respectively.

Among the above dc hysteresis models, when using the look-up-table in the magnetic circuit model, it is possible to calculate the hysteresis loops under sinusoidal and square voltage excitations, while the minor loops cannot be simulated under PWM excitation. On the other hand, when using the simplified LLG

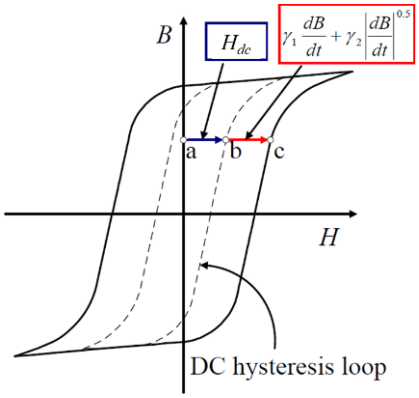

Fig. 2 A schematic diagram of the hysteresis loop under ac excitation.

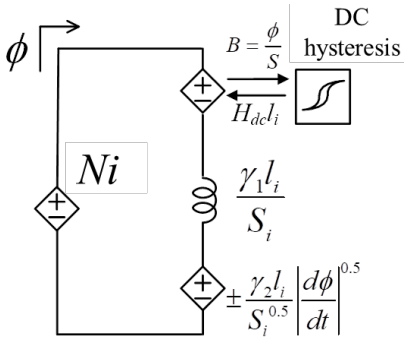

Fig. 3 Magnetic circuit model considering magnetic hysteresis behavior.

equation (the principle and simplification process are explained in the Section 2.4), although the minor loops can be accurately simulated, the calculation time tends to be longer because repeat convergence calculation is indispensable. On the contrary, it is possible to calculate the hysteresis loop with not only high accuracy but also high speed by using the play model (the principle is explained in the Section 2.3).

Next, the identification method of parameters γ_1 and γ_2 is described. Assuming that a flux density waveform is sinusoidal, W_i can be obtained from Eq. (3) as follows:

$$W_i = \frac{1}{Tq_i} \int_{B(t=0)}^{B(t=T)} H_{dc} dB + \frac{2\pi^2 \gamma_1 B_m^2}{q_i} f^2 + 8.763 \frac{\gamma_2 B_m^{1.5}}{q_i} f^{1.5}, \tag{5}$$

where a period is T and mass density is q_i, respectively. Dividing both sides of Eq. (5) by f, the following equation is given:

$$\frac{W_i}{f} = g(B_m) + \frac{2\pi^2 \gamma_1 B_m^2}{q_i} f + 8.763 \frac{\gamma_2 B_m^{1.5}}{q_i} f^{0.5}. \tag{6}$$

where the constant 8.673 is obtained by numerical integration. Here, γ_1 is given by the following equation based on the classical eddy current theory:

$$\gamma_1 = \frac{\sigma d^2}{12}, \tag{7}$$

where conductivity is σ and thickness of a steel sheet is d, respectively. Then, γ_2 can be determined by approximating the core loss curves of core material by using the least squares method based on Eq. (6), as shown in Fig. 4.

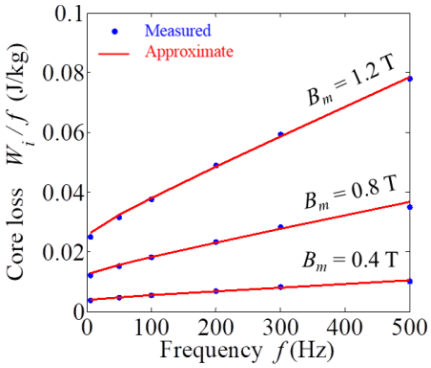

Fig. 4 Measured core loss and its approximate curves of a non-oriented silicon steel with a thickness of 0.35 mm.

2.3 Principle of play model

Fig. 5(a) illustrates a schematic diagram of the play model [9], which is one of phenomenological hysteresis models. In this model, each play hysteron $p_i(x)$, which has different value of width 2ζ and depends on not only the input x but also the past hysteresis as shown in Fig. 5(b), is defined as follows:

$$p_i(x) = \max(\min(p_{i0}, x+\zeta), x-\zeta) \quad (i = 1 \sim N), \tag{8}$$

where a value of $p_i(x)$ in the previous calculation step is p_{i0}. Then, a single-valued shape function $f_i(p_i(x))$, which reflects magnetic properties of arbitrary core material, takes each of $p_i(x)$, and the output y is obtained by the following equation:

$$y = \sum_{i=1}^{N} f_i\left(p_i(x)\right), \tag{9}$$

Here, the shape function is identified from a large number of measured dc hysteresis loops with various maximum flux densities.

The play model can simulate arbitrary hysteresis behavior including complicated minor loops under PWM excitation. Besides, this model has the advantage of fast calculation because no convergence calculation is required. However, the acquisition of a lot of measured data described above has been a large obstacle in practical use.

To overcome the above problem, the efficient method, which obtains the play model from the dc hysteresis loops calculated by the simplified LLG equation, was presented (the specific procedure is explained in the Section 2.5). In this way, only two or three dc hysteresis loops have to be measured [10].

2.4 Principle and simplification process of LLG equation

Micromagnetics is one of physical models based on the LLG equation [16], which can simulate the hysteresis behavior and magnetization distribution inside a magnetic substance. When an analytical region is divided into n elements, the behavior of each magnetization can be represented by the following equation:

$$\frac{d\boldsymbol{m}_i}{dt} = -|\gamma|(\boldsymbol{m}_i \times \boldsymbol{H}_{eff\_i}) + \alpha(\boldsymbol{m}_i \times \frac{d\boldsymbol{m}_i}{dt}) \quad (i = 1 \sim n), \tag{10}$$

where the normalized magnetization vector in each element is $\boldsymbol{m}_i$, the gyromagnetic ratio of electron is γ, the damping constant is α, and the effective field in each

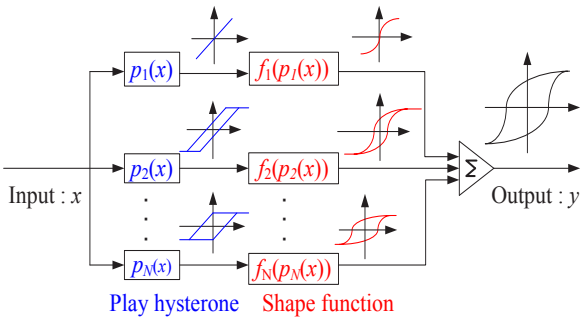

(a) Schematic diagram of the play model.

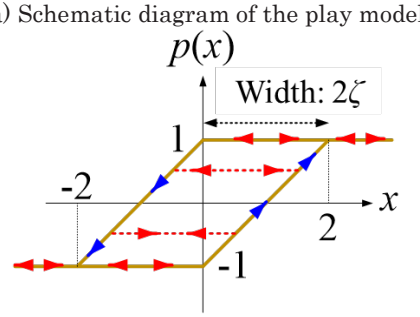

(b) Behavior of the play hysteron.

Fig. 5 Principle of the play model.

element is $\boldsymbol{H}_{eff\_i}$, respectively. $\boldsymbol{H}_{eff\_i}$ is given by the following equation:

$$\boldsymbol{H}_{eff\_i} = \boldsymbol{H}_{app\_i} + \boldsymbol{H}_{ani\_i} + \boldsymbol{H}_{exc\_i} + \boldsymbol{H}_{mag\_i}, \tag{11}$$

where the applied field is $\boldsymbol{H}_{app\_i}$, the anisotropy field is $\boldsymbol{H}_{ani\_i}$, the exchange field is $\boldsymbol{H}_{exc\_i}$, and the magnetostatic field is $\boldsymbol{H}_{mag\_i}$ (including the demagnetizing field), in each element, respectively.

Though the original LLG equation can express micro magnetic phenomena in detail, including the magnetic anisotropy, domain wall motion, and interaction between magnetizations, the micromagnetics model is too large and complicated to be applied to analysis of electric machines. To overcome this issue, Ref. 11) presented a simplified method for approximately expressing the magnetic hysteresis by providing several assumptions.

The first assumption is that originally multi-domain structure in each crystal grain is regarded as single-domain one, to significantly reduce the number of elements and thereby the computer memory. Here, $\boldsymbol{H}_{exc\_i}$, which expresses the domain wall motion, is neglected. On the other hand, since the magnetization reversal due to the domain wall motion cannot be expressed, each magnetization is made easier to rotate by making the coefficient representing strength of the anisotropy field smaller than the actual physical constant.

Next, $\boldsymbol{H}_{mag\_i}$, which expresses the interaction between magnetizations, are approximated as the function of the average normalized magnetization, which is called "the field generated by the magnetoelastic energy", to shorten the calculation time to be practical.

Furthermore, the magnetoelastic effect, internal stress, lattice defect, *etc.* are approximately considered by determining the coefficients of $\boldsymbol{H}_{ani\_i}$ and $\boldsymbol{H}_{ela\_i}$ so as to match the measured hysteresis loop.

From the above, $\boldsymbol{H}_{eff\_i}$ is given by the following equation in the simplified method:

$$\boldsymbol{H}_{eff\_i} = \boldsymbol{H}_{app\_i} + \boldsymbol{H}_{ani\_i} + \boldsymbol{H}_{ela\_i}, \tag{12}$$

where the field generated by the magnetoelastic energy in each element is $\boldsymbol{H}_{ela\_i}$. In Eq. (12), $\boldsymbol{H}_{ani\_i}$ is given by the following equation:

$$\boldsymbol{H}_{ani\_i} = -\frac{\partial}{\partial \boldsymbol{m}_i}\left\{\frac{h_{ani\_i}}{2}\left(a_{1i}^{\ 2}a_{2i}^{\ 2} + a_{2i}^{\ 2}a_{3i}^{\ 2} + a_{3i}^{\ 2}a_{1i}^{\ 2}\right)\right\}, \tag{13}$$

where the coefficient of the anisotropy field is h_{ani_i}, and direction cosines of magnetization vectors with respect to x, y, and z axes (easy axes) of each grain are a_{1i}, a_{2i}, and a_{3i}, in each element, respectively. Here, h_{ani_i} has a normal distribution with the average value of h_{ani} and standard deviation value of σ_{ani}, and easy axes of each magnetization are randomly distributed. h_{ani} and σ_{ani} are determined by the following empirical formulas:

$$h_{ani} = 2.5\sqrt{\frac{M_s}{B_m}}H(B=0), \tag{14}$$

$$\sigma_{ani} = 0.25h_{ani}, \tag{15}$$

where the spontaneous magnetization is M_s. Besides, h_{ani} is smaller than the actual physical constant as mentioned above. On the contrary, $\boldsymbol{H}_{ela\_i}$ is given by the following equation:

$$\boldsymbol{H}_{ela\_i} = -\frac{\partial}{\partial \boldsymbol{m}_i}\left(\frac{1}{M_s}\sum_{j=1}^{n} b_{2j}\bar{m}^{2j}\right), \tag{16}$$

where the generic term of coefficients of Taylor expansion is b_{2j}, and the average normalized magnetization is $\bar{m}$, respectively. Here, b_{2j} is determined by using the Gauss-Newton method so that an error between the measured and calculated hysteresis loops is the smallest. Fig. 6 illustrates the relationship between the parameters h_{ani} and b_{2j}, and a shape of the hysteresis loop. As shown in these figures, the coercive force is proportional to h_{ani}, and the magnetic nonlinearity due to the saturation is represented by b_{2j}, which is determined from a shape of the rising curve in the first quadrant.

2.5 Derivation method of play model by using simplified LLG equation

As described in the Section 2.3, the play model can calculate the dc hysteresis loop with high accuracy and high speed, though a large number of measured dc hysteresis loops with different maximum flux densities are required to derive it. On the other hand, as mentioned in the Section 2.4, the simplified LLG equation can calculate the dc hysteresis loop with arbitrary maximum flux density at high accuracy despite relatively long time. In view of these advantages and disadvantages of both methods, Ref. 10) presented the practical method for deriving the play model by using the simplified LLG equation, and the magnetic circuit model incorporating the obtained play model.

The specific procedure of the proposed method is described below. First, two or three dc hysteresis loops are measured, and the parameters of the simplified LLG equation are determined. Next, a number of dc hysteresis loops with different maximum flux densities are calculated by the simplified LLG equation. Table 1 shows

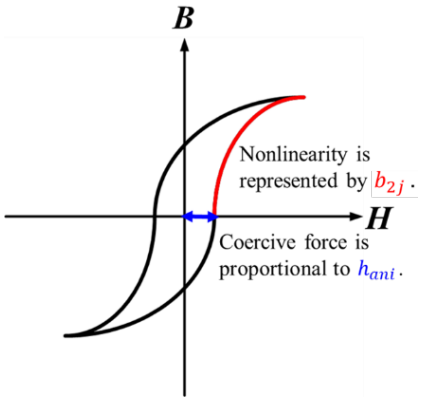

Fig. 6 Relationship between parameters of the simplified LLG equation and a shape of hysteresis loop.

Table 1 Parameters of the simplified LLG equation of a non-oriented silicon steel with a thickness of 0.35 mm.

n	2048	b_8	-7.70×10^4
M_s	1.8	b_{10}	4.13×10^5
h_{ani}	110	b_{12}	-1.30×10^6
σ_{ani}	27.5	b_{14}	2.50×10^6
b_2	1.55×10^2	b_{16}	-2.86×10^6
b_4	-2.65×10^2	b_{18}	1.79×10^6
b_6	7.85×10^3	b_{20}	-4.71×10^5

the parameters of the simplified LLG equation, which are obtained from the measured dc hysteresis loop with B_m = 1.6 T. Fig. 7(a) shows the comparison of measured and calculated dc hysteresis loops. From this figure, it is clear that measured and calculated results are in good agreement. Fig. 7(b) shows a lot of dc hysteresis loops calculated by the simplified LLG equation, which are used to obtain the play model instead of measured ones.

2.6 Simulation results by magnetic circuit model incorporating play model

In Ref. 10), the magnetic circuit model incorporating the play model was proposed and coupled with an electric circuit, as shown in Fig. 8, to calculate the hysteresis loops when a ring core is excited by sinusoidal and PWM voltage. Fig. 9(a) and (b) show the comparison of measured and calculated hysteresis loops under sinusoidal voltage excitation, when B_m = 0.4 T, 0.8 T, and 1.2 T and f = 50 Hz and 300 Hz, respectively. From these figures, it can be seen that measured and calculated results are in good agreement with various maximum flux densities and frequencies. Fig. 10(a) and (b) show the comparison of measured and calculated current waveform and hysteresis loop under PWM voltage excitation. As shown in these figures, the complexly distorted current waveform and the hysteresis loop including the minor loops are almost accurately simulated.

The above-described magnetic circuit model can relatively easily analyze the magnetic hysteresis with

high accuracy and high speed. However, this method can be applied only for the objects with simple shapes such as a ring core, since it is generally difficult to apply the magnetic circuit method to analysis of devices with complicated structure or flux distribution, including an electric motor. Hence, a more detailed model, namely the reluctance network analysis (RNA) model, is necessary. Therefore, in the Chapter 3, the magnetic circuit model incorporating the play model is extended to the RNA, to analyze various kinds of electric machines considering the iron loss caused by the magnetic hysteresis behavior.

3. RNA Model Considering Magnetic Hysteresis Behavior by Incorporating Play Model

The RNA expresses an analytical object by one reluctance network. All the reluctances can be determined by *B*-*H* curve of material and dimensions [17].

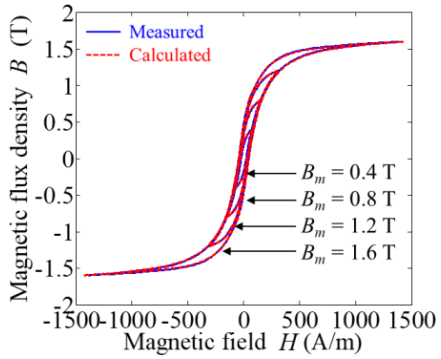

(a) Measured and calculated dc hysteresis loops of a non-oriented silicon steel with a thickness of 0.35 mm.

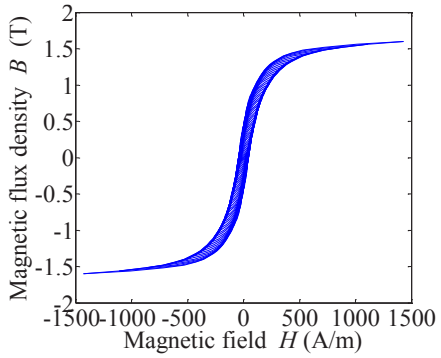

(b) Calculated dc hysteresis loops of a non-oriented silicon steel with a thickness of 0.35 mm from B_m = 0.04 T to 1.6 T at intervals of 0.04 T.

Fig. 7 Calculated dc hysteresis loops by using the simplified LLG equation.

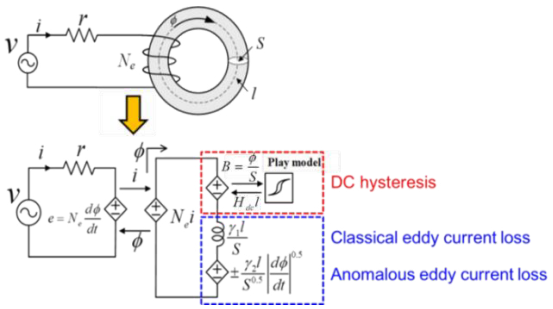

Fig. 8 Magnetic circuit model incorporating the play model.

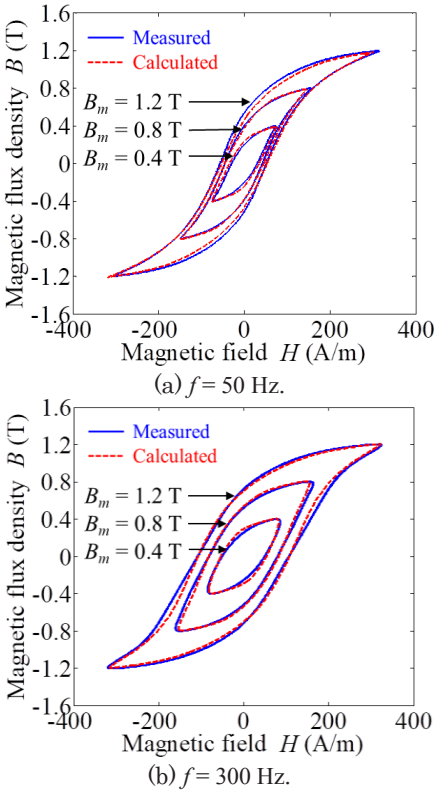

Fig. 9 Calculated hysteresis loops by using the magnetic circuit model incorporating the play model under sinusoidal voltage excitation.

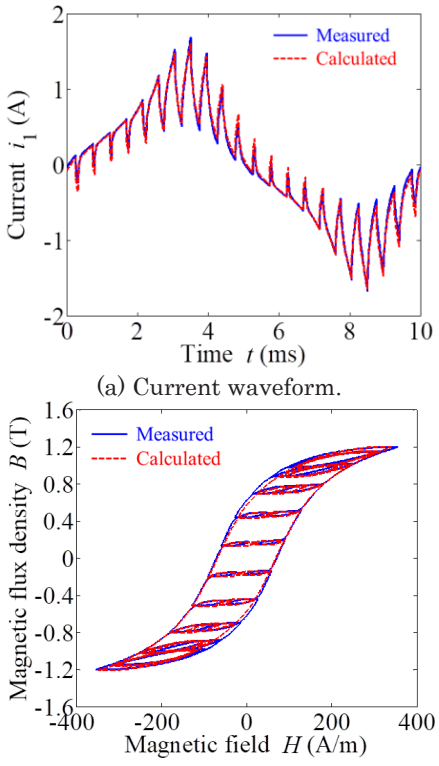

Fig. 10 Calculated current waveform and hysteresis loop by using the magnetic circuit model incorporating the play model under PWM voltage excitation.

The RNA has some advantages such as a simple model, fast calculation, and easy coupling with an external electric circuit and motion equation. In addition, the RNA can express flux distribution inside the analytical object. Thus, the RNA has been applied to the analyses of various kinds of electric machines, including an electric motor [18)-20)].

In this Chapter, the basis of the RNA is explained first, and then the derivation method of the RNA model considering the magnetic hysteresis behavior is described. Ref. 21) and Ref. 22) previously proposed the RNA models incorporating the Preisach model [23)] and Loss Surface (LS) model [24)], respectively, which are ones of phenomenological hysteresis models, and these RNA models are applied to the analyses of permanent magnet (PM) motors. However, these hysteresis models essentially require high computer memory. Moreover, neither RNA models are insufficiently validated because measured and calculated results have never been compared. Therefore, this chapter introduces the RNA model incorporating the above-described play model and some of its analysis examples [25)-28)].

3.1 Basis of RNA

In this section, a conventional method for deriving a two-dimensional (2-D) RNA model is described [17)], taking a cut-core made of a non-oriented silicon steel with a thickness of 0.35 mm shown in Fig. 11(a) as an example.

First, an analytical object, which consists of a core and a peripheral air region, is divided into multiple elements, as shown in Fig. 11(b). Each divided element is represented by a unit magnetic circuit composed of four reluctances, as shown in Fig. 11(c).

Among them, reluctances in a rolling direction are determined in consideration of the magnetic nonlinearity as follows:

$$H = \alpha_1 B + \alpha_m B^m, \tag{17}$$

where coefficients are a_1 and a_m. Also, order m is determined by strength of the nonlinearity of the *B-H* curve. From Eq. (17), a relationship between MMF fm and flux ϕ in each reluctance can be expressed by the following equation:

$$f_m = \left(\frac{\alpha_1 l}{S} + \frac{\alpha_m l}{S^m} \phi^{m-1} \right) \phi, \tag{18}$$

where an average cross-sectional area and magnetic path length of each element are S and l, respectively. Therefore, the nonlinear reluctance $R_{m//}$ is given by the following equation:

$$R_{m//} = \frac{\alpha_1 l}{S} + \frac{\alpha_m l}{S^m} \phi^{m-1}. \tag{19}$$

Next, reluctances perpendicular to a rolling direction are needed to be determined in consideration of flux passing through nonmagnetic layers between steel sheets. In general, the reluctance $R_{m\perp}$ is given by the following equation using the effective permeability μ':

(a) A cut-core used in the examination.

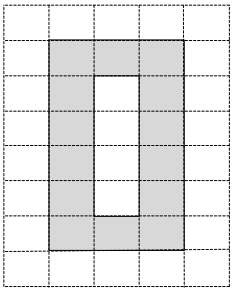

(b) Division of an analytical object.

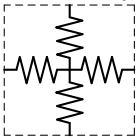

(c) 2-D unit magnetic circuit.

Fig. 11 Conventional derivation method of the RNA model of a cut-core.

$$R_{m\perp} = \frac{l}{\mu' S}. \tag{20}$$

Here, a core is composed of laminated steel sheets with the permeability μ_s and nonmagnetic layers with the vacuum permeability μ_0 at a ratio of d_f : (1-d_f), where a space factor of a core is d_f. Hence, μ' is given by the following equation:

$$\frac{1}{\mu'} = \frac{d_f}{\mu_s} + \frac{1 - d_f}{\mu_0}. \tag{21}$$

If flux flowing perpendicular to laminated steel sheets is so small that the saturation does not occur, μ_s is sufficiently larger than μ_0. Thus, Eq. (21) can be approximated as follows:

$$\frac{1}{\mu'} \cong \frac{1 - d_f}{\mu_0}. \tag{22}$$

Therefore, $R_{m\perp}$ is given by the following equation:

$$R_{m\perp} \cong \frac{(1 - d_f) l}{\mu_0 S}. \tag{23}$$

Moreover, the reluctance R_{ma} in an air region surrounding a core is simply given by the following equation:

$$R_{ma} = \frac{l}{\mu_0 S}. \tag{24}$$

Fig. 12 shows an example of the conventional RNA model. In this figure, MMF generated by winding current

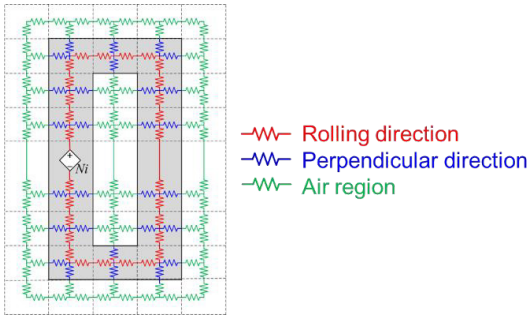

Fig. 12 Conventional RNA model of a cut-core.

is placed in the position where a winding is applied. As shown in this figure, the conventional RNA model consists of only reluctances and MMF. Hence, the magnetic hysteresis behavior is not taken into consideration. Therefore, in the Section 3.2, the play model described in the Chapter 2 is applied to the RNA model.

3.2 RNA model incorporating play model

Fig. 13 shows the RNA model incorporating the play model [25]. In this model, the reluctances in a rolling direction, which are conventionally given by Eq. (19), are represented by the play model and magnetic circuit elements. On the contrary, the reluctances in a perpendicular direction and an air region are given by Eq. (23) and Eq. (24) in the same way as the conventional RNA model, respectively.

Fig. 14(a) and (b) show the comparison of measured and calculated hysteresis loops under sinusoidal voltage excitation, when B_m = 0.4 T, 0.8 T, and 1.2 T and f = 50 Hz and 300 Hz, respectively. From these figures, it is understood that measured and calculated results are in good agreement.

In addition, Fig. 15 indicates the calculated hysteresis loop in a certain divided element of the RNA model. As shown in this figure, the magnetic hysteresis inside a core, which is generally difficult to measure and calculate, can be drawn, though its validity should be experimentally proved.

3.3 Analysis of switched reluctance motor

In the previous research, the RNA model incorporating the play model, which is described in the Section 3.2, has been applied to the analyses of a PM motor [26], three-phase-laminated-core variable inductor [27], and switched reluctance (SR) motor [28]. Among them, the analysis result of the SR motor is reported as a representative in this section.

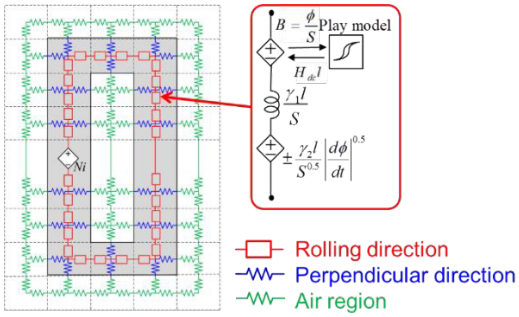

Fig. 13 RNA model of a cut-core incorporating the play model.

Fig. 16 shows specifications of the SR motor with 4-slots and 2-poles used in the examination. The core material is a non-oriented silicon steel with a thickness of 0.35 mm.

Fig. 17 shows a schematic diagram of the RNA model of the SR motor incorporating the play model. The reluctances in stator and rotor cores are given by the play model and magnetic circuit elements. The reluctances between a stator pole and yoke, and between adjacent stator poles, are simply given by Eq. (24). MMF at each stator pole is generated by winding current.

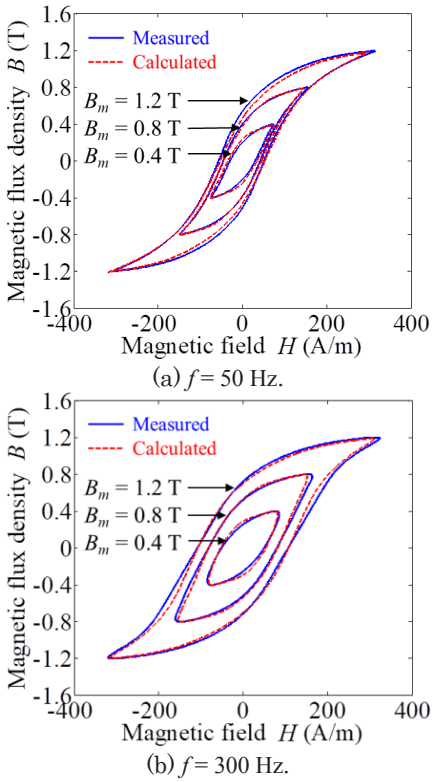

Fig. 14 Calculated hysteresis loops by using the magnetic circuit model incorporating the play model under sinusoidal voltage excitation.

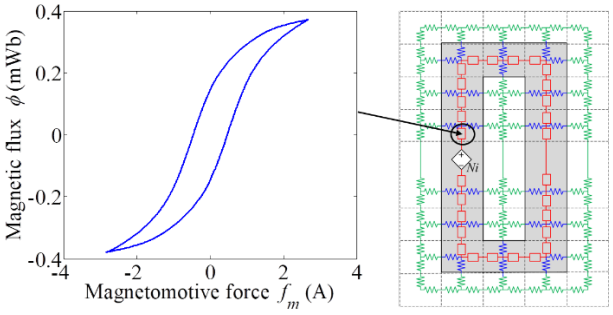

Fig. 15 Calculated Hysteresis loop in a certain divided element of the RNA model.

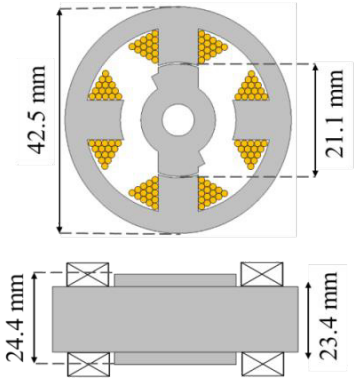

Fig. 16 Specifications of the SR motor used in the examination.

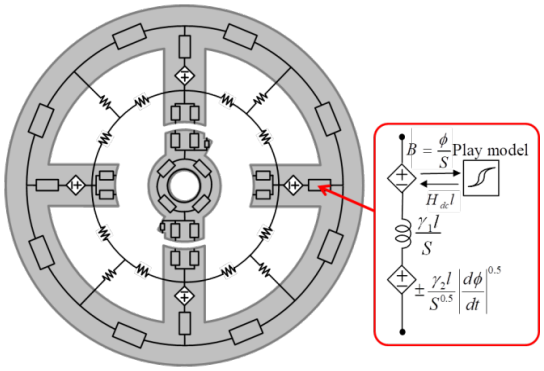

Fig. 17 Schematic diagram of the RNA model of the SR motor incorporating the play model.

In addition, since an SR motor has salient pole structure, flux distribution around stator and rotor pole tips dynamically changes with rotation [18]. Hence, the magnetic circuit around pole tips and air gap is represented by the variable reluctances depending on the rotor position angle as shown in Fig. 18, so that the local saturation and fringing flux can be taken into consideration.

The characteristics of the SR motor are calculated by using the above-described RNA model coupled with an electric circuit, as shown in Fig. 19. Fig. 20 and Fig. 21 show the comparison of measured and calculated iron loss and winding current density versus torque characteristics, respectively. Here, the calculated iron loss is obtained by subtracting machine output, and copper and mechanical losses from electrical input. From these figures, it can be seen that measured and calculated values are almost in good agreement. However, it is not commonly seen in an SR motor that the calculated iron loss is reduced due to increasing the torque. The cause of this tendency is considered to be that the machine output, which is the product of torque and rotational speed, is two orders larger than iron loss so that a slight error of the torque can subordinately affect the iron loss value.

Furthermore, as shown in Fig. 22, this RNA model can draw such distorted or dc-biased hysteresis loops in certain divided elements, even though they should be validated by the experiment.

4. Magnetic Circuit Model Considering Dynamic Hysteresis Characteristics by Incorporating Play Model and Cauer Circuit

The above-described magnetic circuit and RNA

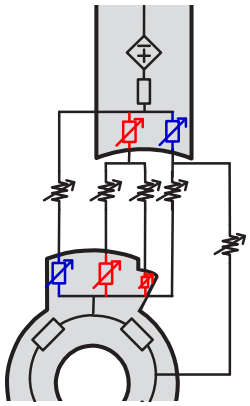

Fig. 18 Magnetic circuit around pole tips and air gap.

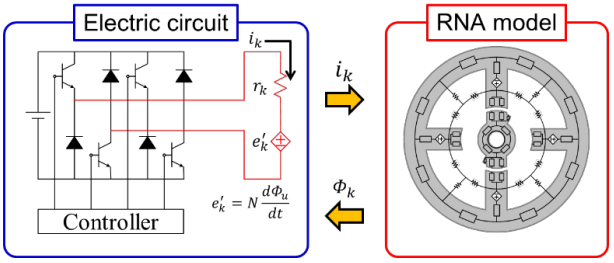

Fig. 19 Electric- and magnetic- coupled model of the SR motor.

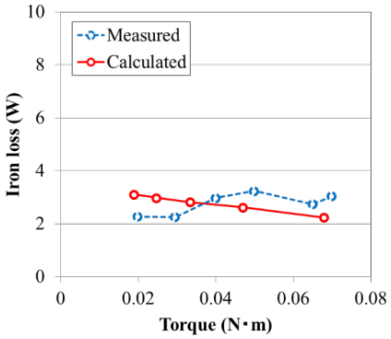

Fig. 20 Measured and calculated iron loss characteristics.

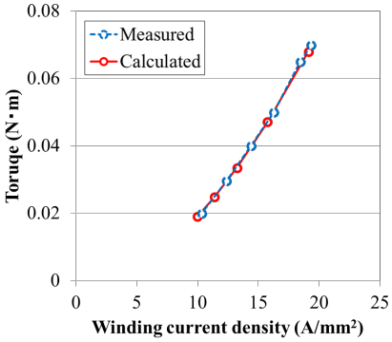

Fig. 21 Measured and calculated winding rms current versus torque characteristics.

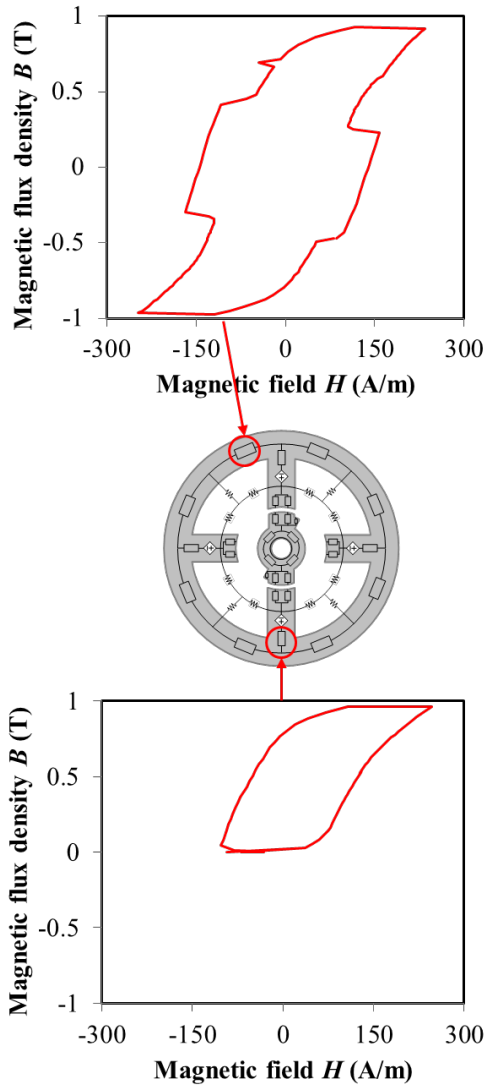

Fig. 22 Hysteresis loops in certain divided elements of the RNA model of the SR motor.

methods incorporating the play model can analyze the magnetic hysteresis with high accuracy and high speed by using relatively simple models, However, they cannot consider the influence of the skin effect because the classical eddy current loss is denoted by just a single inductance element based on the classical eddy current theory. Therefore, there is a possibility for further improvement in the calculation accuracy of the hysteresis loop at a high frequency, such as when including the minor loops generated from carrier harmonics under PWM excitation, as shown in Fig. 23(a) and (b). Here, a ring core made of a grain-oriented silicon steel with a thickness of 0.23 mm is used in the examination. In this chapter, it should be noted the play model is derived from only the measured dc hysteresis loops, to more accurately verify the calculation accuracy by eliminating errors due to the simplified LLG equation.

To practically analyze taking the skin effect into account, some kind of approximate calculation is required, since it is not realistic to perform a three-dimensional (3-D) analysis by modeling each laminated

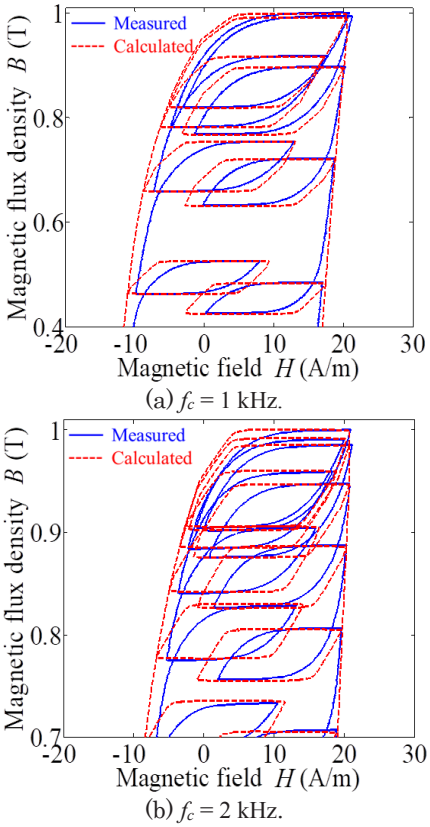

Fig. 23 Enlarged views of measured and calculated hysteresis loops under PWM voltage excitation (the classical eddy current is represented by a single inductance element).

steel sheet from the viewpoint of calculation time and computer memory. So far, various kinds of methods for calculating the classical eddy current loss considering the influence of the skin effect have been proposed for the FEM.

One of typical methods is a one-dimensional (1-D) eddy current analysis in the thickness direction for each mesh as the post-processing based on the result of the main 2-D FEM, to obtain loss distribution inside a steel sheet [29]. Further, this post 1-D analysis can be implemented by simultaneously using the play model to express the dc hysteresis (this method is called "P1D method" in the following) [30].

Another representative model of the skin effect is the Cauer circuit [31), 32)], which is a ladder-type electric equivalent circuit composed of multiple resistance and inductance elements connected in series and in parallel as shown in Fig. 24. Using the Cauer circuit, the 1-D electromagnetic field analysis can be performed by considering the frequency characteristic of the complex permeability. In Ref. 33), the 1-D analysis is conducted by combining the play model and Cauer circuit, when a ring core is excited by PWM voltage. It was clear that the hysteresis loop including the minor loops and iron loss can be calculated with high accuracy. Moreover, in Ref. 34), the post 1-D analysis is implemented by using the play model and Cauer circuit for each mesh, after the main 2-D analysis incorporating the play model for a PM motor. Compared with the above-described P1D method,

this method has the same calculation accuracy and can significantly reduce the calculation time. This is because the Cauer circuit requires low computer memory since each mesh of the main FEM model is just given by a simple electric equivalent circuit, while each mesh must be further divided into multiple elements in the thickness direction according to the skin depth in the P1D method.

As described above, various studies for modeling the skin effect have been conducted. However, none of those methods has been sufficiently studied because there are few examples of application to the 3-D analysis. Besides, since these methods have been used only for the post-processing, it is desired to establish a more practical method which can take the skin effect into account during the electromagnetic field analysis.

Therefore, this chapter introduces the magnetic circuit model considering the dynamic hysteresis characteristics including the skin effect, by incorporating the Cauer circuit in addition to the play model [35]. In the following, it is revealed that this model is improved in the calculation accuracy of the minor loops, compared to the previous one.

4.1 Derivation of magnetic circuit model incorporating play model and Cauer circuit

Fig. 24 shows a schematic diagram of the Cauer circuit, as explained above. The dc magnetization is represented by the first inductance L_0, and the frequency characteristic of the complex permeability due to the classical eddy current is represented by the part of the first resistance R_0 and after. For practical use, the theoretically infinite stages of the ladder circuit should be truncated to finite stages. The frequency characteristic including the skin effect at a higher frequency can be expressed as the number of circuit stages is larger [31), 32)]. The parameters L and R in the circuit are given by the following equations:

$$L = \mu, \tag{25}$$

$$R = \frac{4}{\sigma d^2}, \tag{26}$$

where the dc permeability is μ. Here, the units of L and R are H/m and Ω/m, respectively. From Eq. (7) and Eq. (26), it is understood that R_0 (= $3R$) is equivalent to the inverse of γ_1. Although the Cauer circuit cannot express the dc hysteresis and anomalous eddy current loss in general, the improved model shown in Fig. 25 can take them into consideration [33)].

In the magnetic circuit model incorporating the play model, which is described in the Chapter 2, the relationship between H and B is given by Eq. (3). On the other hand, in the Cauer circuit presented in Ref. 33), the

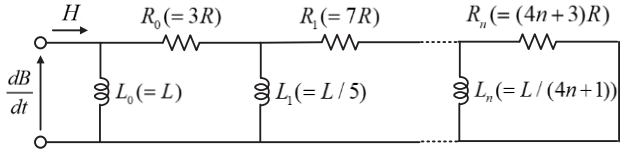

Fig. 24 Schematic diagram of the Cauer circuit.

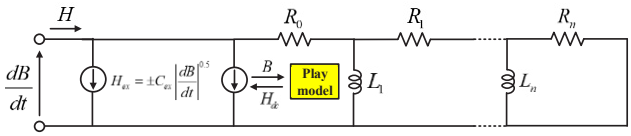

Fig. 25 Cauer circuit taking the dc hysteresis and anomalous eddy current loss into consideration.

relationship between H and B is given by the following equations in case of the number of circuit stages is one and more:

$$H = H_{dc} + \frac{1}{3R}\frac{dB}{dt} \pm C_{ex}\left|\frac{dB}{dt}\right|^{0.5} \qquad (n = 0), \tag{27}$$

$$H = H_{dc} + \left\{\sum_{i=1}^{n}\left(\frac{B_i}{L_i}\right) + \frac{1}{R_n}\left(\frac{dB_n}{dt}\right)\right\} \pm C_{ex}\left|\frac{dB}{dt}\right|^{0.5} \qquad (n \geq 1), \tag{28}$$

Comparing Eq. (3), Eq. (27), and Eq. (28), the first terms, which are represented by the play model, and the third ones, which are given by the product of $|dB/dt|^{0.5}$ and the coefficient determined by the core loss curves, are equivalent, respectively. Next, the second terms are equivalent in Eq. (3) and Eq. (27) because they both represent the classical eddy current loss caused by the main flux and are given by the product of dB/dt and the coefficient based on the classical eddy current theory. On the other hand, not only the classical eddy current loss due to the main flux but also the influence of the skin effect are expressed in Eq. (28). Hence, the calculation accuracy of the magnetic circuit model at a high frequency can be improved by making it equivalent to Eq. (28). However, it is difficult to express this with just a single magnetic circuit element.

Therefore, Ref. 35) presented the magnetic circuit model incorporating the Cauer circuit theory as well as the play model, as shown in Fig. 26. In this model, the classical eddy current loss including the influence of the skin effect is represented by coupling the magnetic circuit with the ladder circuit, which is equivalent to the part of R_0 and after in the Cauer circuit.

4.2 Simulation results by magnetic circuit model incorporating play model and Cauer circuit

Fig. 27(a) and (b) show enlarged views of the comparison of measured and calculated hysteresis loops under PWM voltage excitation at carrier frequencies f_c = 1 kHz and 2 kHz, respectively. Here, the ladder circuit is terminated by the second stage, that is, the second resistance R_1. From these figures, it is understood that the calculation accuracy of the minor loops is further improved compared to the calculation result shown in Fig. 23.

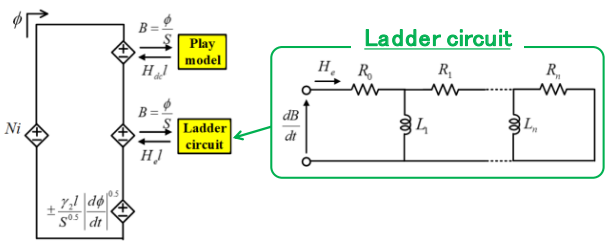

Fig. 26 Magnetic circuit model incorporating the play model and Cauer circuit.

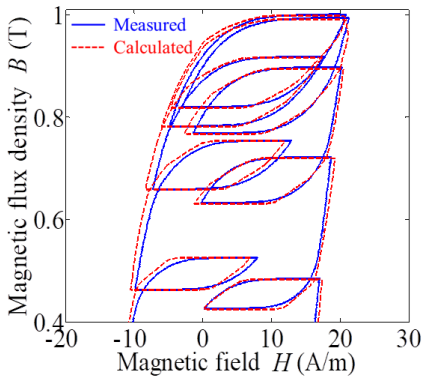

(a) f_c = 1 kHz.

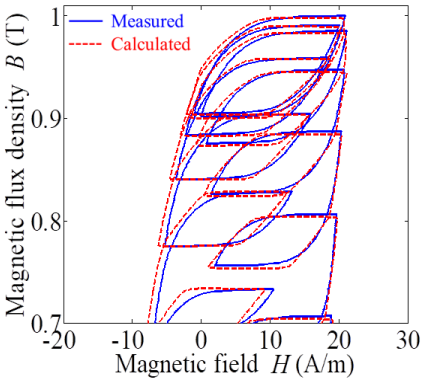

(b) f_c = 2 kHz.

Fig. 27 Enlarged views of measured and calculated hysteresis loops under PWM voltage excitation (the classical eddy current is represented by the ladder circuit).

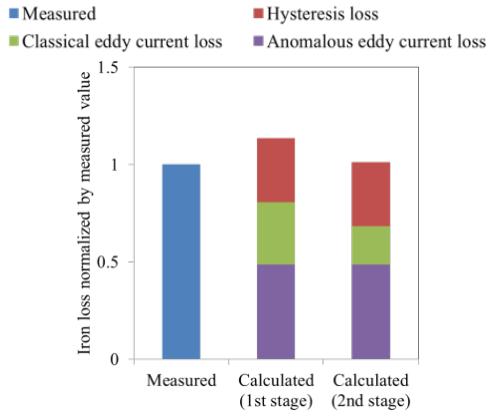

(a) f_c = 1 kHz.

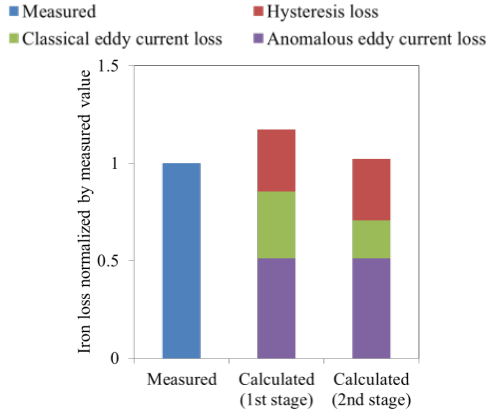

(b) f_c = 2 kHz.

Fig. 28 Measured and calculated iron loss normalized by measured values.

Fig. 28(a) and (b) show the comparison of measured and calculated iron loss normalized by the measured values. Here, the ladder circuit is terminated by the first and second stages, that is, the second resistance R_0 and R_1. The figures reveal that the classical eddy current loss is reduced when the ladder circuit is terminated by the second stage, which leads to calculating the iron loss with higher accuracy. The cause of this result is that the effective resistance in a steel sheet increases and the classical eddy current decreases since the eddy current path becomes narrower due to the skin effect.

Furthermore, to validate the magnetic circuit model in more detail, the measured and calculated frequency characteristics of the complex permeability, which are obtained from the measured and calculated hysteresis loops with B_m = 0.3 T from f = 10 Hz to 2 kHz, are compared. Fig. 29(a) and (b) show the comparison of real and imaginary parts of the relative complex permeability. As shown in these figures, the real part can be expressed with higher accuracy at high frequencies when the ladder circuit is terminated by the second stage, while the accuracy of the imaginary part is high regardless of the number of circuit stages. The result of the imaginary part contradicts the above-mentioned improved accuracy of the iron loss calculation since the imaginary part physically means the iron loss. The cause of this result is not clear at present and should be investigated in the future.

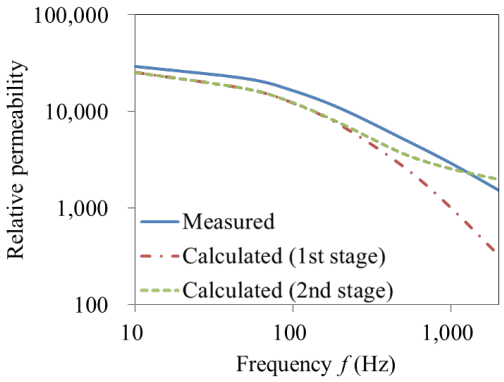

(a) Real part.

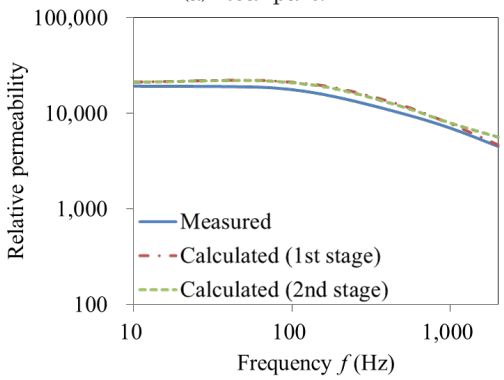

(b) Imaginary part.

Fig. 29 Measured and calculated frequency characteristics of the complex permeability.

5. Modeling Method of Deteriorated Magnetic Properties in Core Material due to Machining Process by Simplified LLG Equation

Magnetic properties of core material are often deteriorated in machining process, which leads to the performance worsening of electric machines. Therefore, the establishment of an analytical method taking deterioration of magnetic properties due to machining process into consideration and the optimization of processing method of core material are essential to development of high-efficiency electric machines.

So far, various kinds of analytical methods considering the deteriorated properties caused by mechanical stress and shrink fitting have been proposed mainly in Japan [36)-39)]. However, these methods have a practical problem that a large number of experimental data should be acquired by using several cores to which different magnitudes of stress is applied. Moreover, most methods only change the reluctivity and loss coefficient of core material depending on the magnitude of stress, and none of them can accurately simulate considering change in a shape of the hysteresis loop. On the contrary, in Ref. 40), magnetic properties of core material are predicted when arbitrary compressive stress is applied, by formulating the simplified LLG equation, described in the Chapter 2, considering the influence of stress. In this method, only the measured data of core material, when no stress is applied, is required. On the other hand, in this method, although the tendency of the iron loss to increase with stress can be expressed, the calculation accuracy is not sufficiently high (e.g., up to about 1.5 times of larger calculated values of iron loss than measured ones).

To resolve the above problems, it is necessary to establish a practical and accurate prediction method of deteriorated magnetic properties under arbitrary stress from the minimum essential amount of measured data. Therefore, this chapter introduces that the simplified LLG equation is used for the prediction of deteriorated magnetic properties of arbitrary rolled non-oriented silicon steels from a small amount of measured data of the dc hysteresis loops [41)].

5.1 Deterioration prediction method by simplified LLG equation

Table 2 and Fig. 30 show specifications and dimensions of tested samples used for measurement. The sample No. 0 is an unrolled one, and the ones No. 1~4 are rolled by applying stresses with different magnitudes so that each one has a different thickness. The rolled ratio, shown in Table 2, represents a reduction rate of a thickness of each rolled sample relative to the unrolled one. Fig. 31 shows the measured dc hysteresis loops with B_m = 1.0 T for each sample. As shown in these figures, a shape of the hysteresis loop remarkably changes from the original state in machining process.

In Ref. 41), the relationship between the rolled ratio and the parameters of the simplified LLG equation h_{ani} and b_{2j}, which determines a shape of the hysteresis loop as shown in Fig. 6, is focused on. Table 3 shows the

Table 2 Specifications of test samples.

Sample No.		0	1	2	3	4
Rolled ratio	%	0	3	6	9	12
Density	kg/m^3	7600				

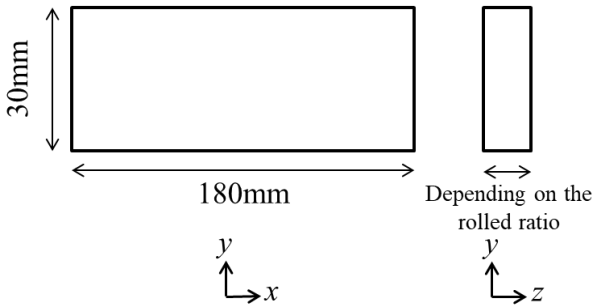

Fig. 30 Dimensions of test samples.

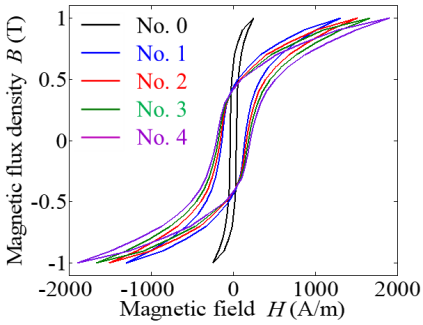

Fig. 31 Measured dc hysteresis loops of each samples with B_m = 1.0 T.

Table 3 Parameters of the simplified LLG equation of samples No. 0~4.

No.	0	1	2	3	4
h_{ani}	109	404	471	546	611
b_2	−1.51	2.86×10^2	3.43×10^2	4.41×10^2	5.00×10^2
b_4	8.21×10^2	2.24×10^3	2.80×10^3	3.04×10^3	3.65×10^3
b_6	-1.61×10^4	5.76×10^3	5.74×10^3	6.01×10^3	6.12×10^3
b_8	2.10×10^5	-1.24×10^4	-1.28×10^4	-1.35×10^4	-1.42×10^4
b_{10}	-1.39×10^6	9.50×10^3	9.60×10^3	9.85×10^3	1.05×10^4
b_{12}	5.39×10^6	-	-	-	-
b_{14}	-1.28×10^7	-	-	-	-
b_{16}	1.83×10^7	-	-	-	-
b_{18}	-1.44×10^7	-	-	-	-
b_{20}	4.78×10^6	-	-	-	-

calculated parameters of the simplified LLG equation, and Fig. 32(a) – (e) show enlarged views of the calculated dc hysteresis loops using the parameters shown in this table. From these table and figure, it is understood that measured and calculated results are in good agreement for each sample.

First, the prediction method of h_{ani} is explained by using the values shown in Table 3. Fig. 33 shows the relationship between the rolled ratio x and h_{ani} of each sample. From these figures, it seems that h_{ani} monotonically increases as x increases. Here, to predict h_{ani} at the arbitrary rolled ratio, $h_{anir}(x)$, which is the ratio

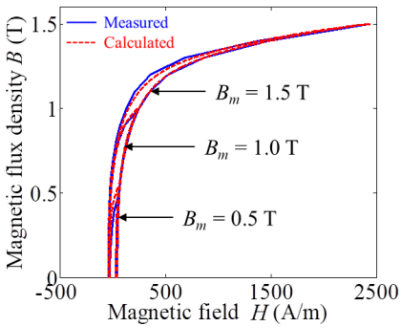

(a) No. 0

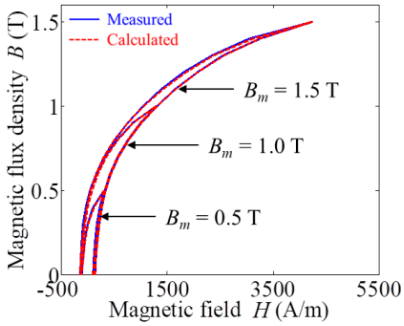

(b) No. 1

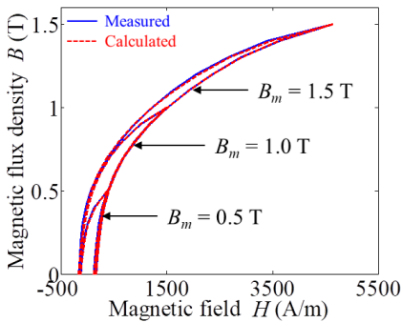

(c) No. 2

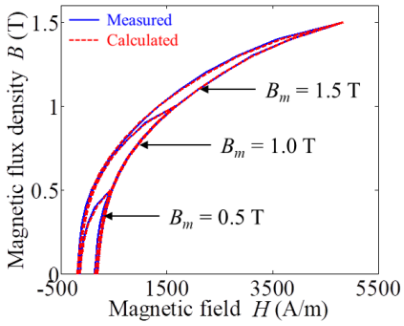

(d) No. 3

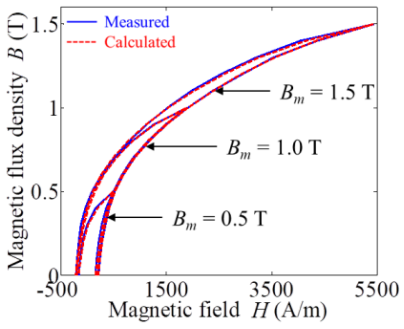

(e) No. 4

Fig. 32 Measured and calculated dc hysteresis loops of each sample.

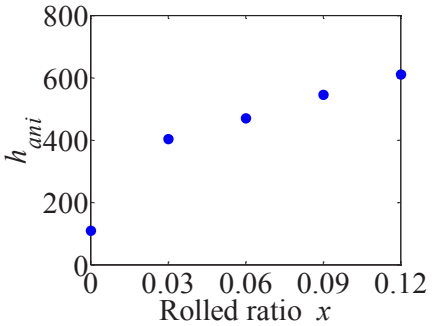

Fig. 33 Relationship between x and h_{ani}.

of h_{ani} of rolled and unrolled samples, is defined as the function of x as follows:

$$h_{anir}(x) = \frac{h_{ani}(x)}{h_{ani}(0)}. \tag{29}$$

Fig. 34 shows the relationship between x and $h_{anir}(x)$. As shown in this figure, $h_{anir}(x)$ changes almost linearly at the rolled ratio of from 3% to 12%. Therefore, can be approximated by the following linear function:

$$h_{anir}(x) = \alpha x + \beta, \tag{30}$$

where coefficients are α and β. It may be possible to predict h_{ani} at the arbitrary rolled ratio by using Eq. (30), though it is necessary to consider how to function $h_{anir}(x)$ at the rolled ratio of from 0% to 3% in the future.

Next, the prediction method of b_{2j} is explained. Fig. 35(a) – (e) show the relationships between x and b_2~b_{10} of each sample. From these figures, it is revealed that b_2~b_{10} do not monotonically change with respect to x, unlike the case of h_{ani}. Hence, since it is difficult to give the relationship between x and b_2~b_{10} by a simple relational expression, it is necessary to predict b_2~b_{10} in another way. Here, b_2~b_{10} express the nonlinearity of the rising curve in the first quadrant as described above, that is to say, b_2~b_{10} of the rolled samples can be determined by predicting the nonlinearity of their hysteresis loops. Thus, $g(B)$, which is the function of B, is defined as follows:

$$g(B) = \frac{1}{h_{anir}} \times \frac{H_{pre}(B)}{H_{nonpre}(B)}, \tag{31}$$

where the magnetic field on the ascending curve of the hysteresis loops of rolled and unrolled samples, where B is positive, is $H_{pre}(B)$ and $H_{nonpre}(B)$, respectively. Fig. 36 shows $g(B)$ derived for each sample and average values.

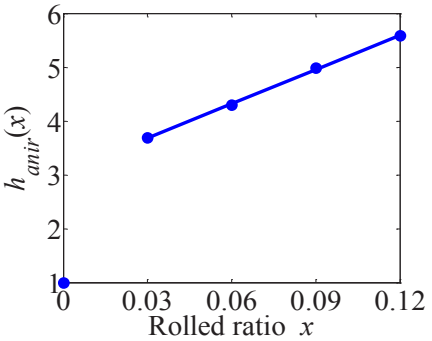

Fig. 34 Relationship between x and $h_{anir}(x)$.

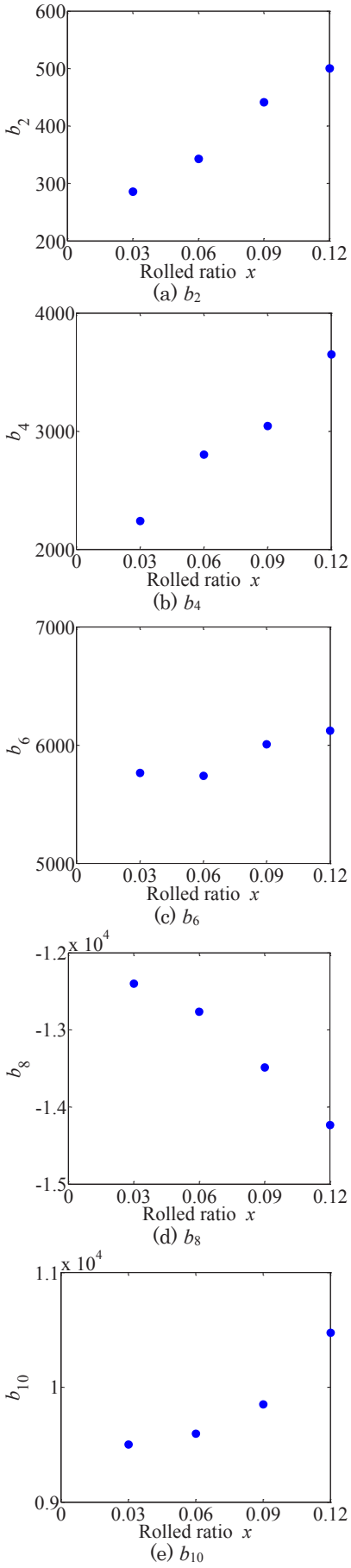

Fig. 35 Relationship between x and b_2~b_{10}.

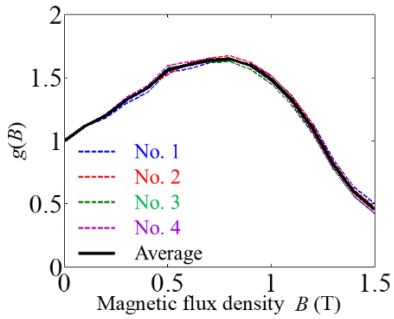

Fig. 36 Relationship between B and $g(B)$.

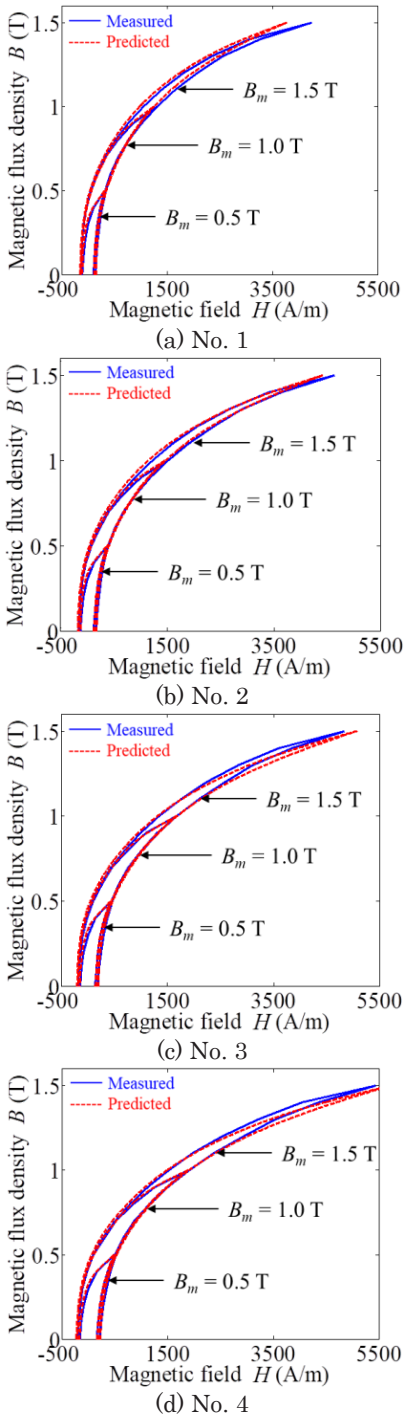

Fig. 37 Measured and predicted dc hysteresis loops of each sample.

From these figures, it is understood that $g(B)$ of each sample has almost same values regardless of x. Hence, $g_{ave}(B)$, which is the average of $g(B)$ of each sample, can be approximated as the polynomial function as follows:

$$g_{ave}(B) = aB^5 + bB^4 + cB^3 + dB^2 + eB + 1, \qquad (32)$$

where coefficients are a, b, c, d, and e. Substituting Eq. (32) into Eq. (31), the following equation can be obtained:

$$H_{pre}(B) = h_{anir} \times H_{nonpre}(B) \times g_{ave}(B). \qquad (33)$$

Therefore, the nonlinearity of the rising curve of the hysteresis loop of the arbitrary rolled sample can be predicted by calculating $H_{pre}(B)$ using Eq. (33).

The predicted dc hysteresis loops are compared with the measured ones, to confirm the validity of the proposed method, as shown in Fig. 37(a) – (d). These figures clarify that measured and predicted results are almost in good agreement for each sample.

Moreover, in Ref. 42), the prediction method in the case of higher rolled ratio is examined and its validity is indicated, though that is omitted in this paper.

6. Conclusion

This paper presented various studies on the hysteresis modeling for electric machines based on the magnetic circuit method. It was clear that the iron loss including the magnetic hysteresis behavior can be calculated at high accuracy with a relatively simple model based on the RNA, even for machines with complex shapes such as an electric motor. In addition, it was found that the magnetic circuit analysis considering the skin effect and the deterioration prediction of machined core's magnetic properties are possible, so that further improvement in the calculation accuracy of the RNA is expected by incorporating them. Furthermore, the proposed method does not require a high-performance computer for conducting a large-scale numerical analysis and special experimental equipment for measuring a lot of hysteresis loops with high accuracy, hence it will be one of the practical solutions for design and analysis of electric machines.

Acknowledgements This work was supported by Grant-in-Aid for JSPS Fellows (JP19J20572).

References

1) C. P. Steinmetz, *Proc. IEEE*, **72**, 197 (1984).
2) G. Bertotti, *IEEE Trans. Magn.*, **24**, 621 (1988).
3) K. Venkatachalam, C. R. Sullivan, T. Abdallah, and H. Tacca, *Conf. Proc. IEEE*, 36 (2002).
4) S. Yanase, H. Kimata, Y. Okazaki, and S. Hayashi, *IEEE Trans. Magn.*, **41**, 4365 (2005).
5) W. Shen, F. Wang, D. Borovevich, and C. W. Tipton, *IEEE Trans. Power Electron.*, **23**, 475 (2008).
6) D. C. Jiles and D. L. Atherton, *J. Magn. Magn. Mater.*, **61**, 48 (1986).
7) G. Friedman, *J. Appl. Phys.*, **67**, 5361 (1990).
8) G. S. Park, S. Y. Hahn, K. S. Lee, and H. K. Jung, *IEEE Trans. Magn.*, **29**, 1542 (1993).
9) S. Bobbio, G. Miano, C. Serpico, and C. Visone, *IEEE Trans. Magn.*, **33**, 4417 (1997).
10) H. Tanaka, K. Nakamura, and O. Ichinokura, *J. Phys: Conf. Series*, **903**, 012047 (2017).
11) H. Oshima, Y. Uehara, K. Shimizu, K. Inagaki, A. Furuya, J. Fujisaki, M. Suzuki, K. Kawano, T. Mifune, T. Matsuo, K. Watanabe, and H. Igarashi, *J. Jpn. Soc. Powder Metallurgy*, **61**, S238 (2013).
12) H. Tanaka, K. Nakamura, and O. Ichinokura, *J. Magn. Soc. Jpn.*, **39**, 65 (2015).
13) H. Tanaka, K. Nakamura, and O. Ichinokura, *J. Phys: Conf. Series*, **903**, 012048 (2017).
14) V. Karapetoff, The Magnetic Circuit (McGraw-Hill, New York (1911).
15) K. Fujita, K. Nakamura, and O. Ichinokura, *J. Magn. Soc. Jpn.*, **37**, 44 (2013).
16) Y. Nakatani, Y. Uesaka, and N. Hayashi, *Jpn. J. Appl. Phys.*, **28**, 2485 (1989).
17) K. Nakamura and O. Ichinokura, *IEEJ Trans. FM*, **128**, 506 (2008).
18) K. Nakamura, K. Kimura, and O. Ichinokura, *J. Magn. Magn. Mater.*, **290-291**, 1309 (2005).
19) M. Fukuoka, K. Nakamura, and O. Ichinokura, *IEEE Trans. Magn.*, **47**, 2414 (2011).
20) K. Nakamura, K. Honma, T. Ohinata, K. Arimatsu, T. Shirasaki, and O. Ichinokura, *J. Magn. Soc. Jpn.*, **38**, 174 (2014).
21) N. Li, J. Zhu, M. Lin, G. Yang, Y. Kong, and L. Hao, *IEEE Trans. Magn.*, **55**, 7203104 (2019).
22) O. Messal, F. Dubas, R. Benlamine, A. Kedous-Lebouc, C. Chillet, and C. Espanet, *Preprints* (2017).
23) G. S. Park, S. Y. Hahn, K. S. Lee, and H. K. Jung, *IEEE Trans. Magn.*, **29**, 1542 (1993).
24) T. Chevaliea, A. Kedous-Lebouc, B. Cornut, and C. Cester, *Physica B*, **275**, 197 (2000).
25) Y. Hane, H. Tanaka, and K. Nakamura, *Trans. Magn. Special Issues*, **2**, 25 (2018).
26) Y. Hane and K. Nakamura, *Conf. Proc. IEEE*, 1800038 (2018).
27) Y. Hane, K. Nakamura, T. Ohinata, and K. Arimatsu, *IEEE Trans. Magn.*, **55**, 8401306 (2019).
28) Y. Hane, K. Mitsuya, and K. Nakamura, *Conf. Proc. IEEE* , 2100016 (2021).
29) K. Yamazaki and N. Fukushima, *IEEE Trans. EC*, **25**, 633 (2010).
30) Y. Takeda, Y. Takahashi, K. Fujiwara, A. Ahagon, and T. Matsuo, *IEEE Trans. Magn.*, **51**, 7300504 (2015).
31) Y. Shindo and O. Noro, *IEEJ. Trans. FM*, **134**, 173 (2014).
32) Y. Shindo, A. Kameari, and T. Matsuo, *PE*, **137**, 162 (2017).
33) I. Suehiro, T. Mifune, T. Matsuo, J. Kitao, T. Komatsu and M. Nakano, *IEEE Trans. Magn.*, **54**, 7300704 (2018).
34) N. Minowa, Y. Takahashi, and K. Fujiwara, *IEEE Trans. Magn.*, **55**, 7401404 (2019).
35) Y. Hane and K. Nakamura, *IEEE Trans. Magn.*, **56**, 6703306 (2020).
36) K. Fujisaki, R. Hirayama, T. Kawachi, S. Satou, C. Kaidou, M. Yabumoto, and T. Kubota, *IEEE Trans. Magn.*, **43**, 1950 (2007).
37) D. Miyagi, K. Miki, M. Nakano, and N. Takahashi, *IEEE Trans. Magn.*, **46**, 318 (2010).
38) K. Yamazaki and W. Fukuoka, *IEEE Trans. Magn.*, **51**, 8102004 (2015).
39) K. Yamazaki and A. Aoki, *IEEE Trans. Magn.*, **52**, 2000704 (2016).
40) A. Furuya, J. Fujisaki, Y. Uehara, K. Shimizu, H. Oshima, and T. Matsuo, *IEEE Trans. Magn.*, **50**, 7300604 (2014).
41) Y. Hane, K. Nakamura, T. Yoshioka, T. Kawase, and T. Ishikawa, *Trans. Magn. Special Issues*, **3**, 64 (2019).
42) Y. Hane, K. Nakamura, T. Kawase, N. Hosokawa, and N. Kurimoto, *Trans. Magn. Special Issues*, **4**, 57 (2020).

Received Sep. 23, 2021; Accepted Dec. 10, 2021

J. Magn. Soc. Jpn., **46**, 37-41 (2022)

<Paper>

3D magnetic field vector measurement by magneto-optical imaging

H. Sakaguchi, R. Oya. S. Wada*, T. Matsumura*, H. Saito*, and T. Ishibashi

Department of Materials Science and Technology, Nagaoka University of Technology, *1603-1 Kamitomioka, Nagaoka, Niigata 940-2188, Japan*

*Department of Mathematical Science and Electrical-Electronic-Computer Engineering, Akita University, *1-1 Tegata Gakuen-machi, Akita 010-8502, Japan*

Magneto-optical (MO) imaging using MO imaging plates is a magnetic imaging technique that enables real-time measurements and is expected to be used for non-destructive testing and for observing the magnetic domains of magnetic materials. In this study, we propose a quantitative measurement method for three dimensional (3D) magnetic field vector measurements. The x- and y-components of the magnetic fields within the measured plane are calculated from the measured z-component by using a signal transformation method based on magnetic field transfer functions. Furthermore, the magnetic field distributions at different heights are also obtained from a one-shot image. In this paper, 3D magnetic field vector measurements are demonstrated for ferrite magnets and an electrical steel sheet.

Key words: magneto-optical imaging, MO imaging plate, polarization camera, magnetic field vector

1. Introduction

Magneto-optical (MO) imaging using an MO imaging plate is a technique to visualize a strayed magnetic field by utilizing the MO effects [1)-11)]. By using bismuth-substituted iron garnets, which exhibit a large Faraday effect in the visible light region, as the MO imaging plate, observation of magnetic domains in magnetic materials and in-situ observation of magnetic flux quanta in superconductors [12)] have been realized with high spatial resolution and magnetic field sensitivity [9)]. In addition, it is attracting attention as a large area magnetic measurement technology that could replaces the scanning hall probe method [13)], since the large MO imaging plates using large glass substrates have been developed [14)-17)]. In MO imaging, it is necessary to calibrate the magnetic field from the light intensity in order to quantitatively measure the magnetic field distribution, although it is a simple method that can be measured using an optical system like a polarizing microscope. Jooss et al. have proposed a method to calibrate the magnetic field from the light intensity in the crossed Nicol method, in which the large number of parameters to be measured beforehand [4), 5)]. We proposed the circular polarization modulation method to quantitatively measure the rotation angle and the ellipticity simultaneously, which can be applied to the MO imaging [6)]. However, it was difficult to realize the real-time measurement because three images measured with linearly-, right circularly- and left circularly-polarizations had to be measured.

In this paper, we report on an MO imaging technique that quantitatively measures the magnetic field distribution from the one-shot image measured using the polarization camera that has been widely used in the industry in recent years. We also report on a signal transformation method that calculates the magnetic field vectors from a measured MO image. In this paper, measurements of the magnetic field distributions of ferrite magnets are demonstrated. A measurement of an electrical steel sheet is also demonstrated.

Corresponding author: T. Ishibashi (e-mail: t_bashi@mst.nagaokaut.ac.jp).

2. Methods

2.1 MO imaging using the polarization camera

The polarization camera is a camera having a structure that integrates an image sensor with a micro-polarizer array consisting of multiple polarizers with different angles of polarization, 0°, 45°, 90° and 135°, formed according to the pixel size [18)]. Therefore, four different polarization images with polarization angles of 0°, 45°, 90° and 135° are measured with one-shot measurement.

This means that rotation angles of polarization are quantitatively measured with a one-shot measurement using the polarization camera. Consequently, once four polarization images with intensities $(I_{0°}, I_{45°}, I_{90°}, I_{135°})$, we can obtain the Stokes parameter, s_0, s_1 and s_2 as described by

$$\begin{pmatrix} s_0 \\ s_1 \\ s_2 \end{pmatrix} = \begin{pmatrix} (I_{0°} + I_{45°} + I_{90°} + I_{135°})/2 \\ I_{0°} - I_{90°} \\ I_{45°} - I_{135°} \end{pmatrix}. \quad (1)$$

The relation between the Stokes parameter and the polarization state is defined by

$$\begin{pmatrix} s_0 \\ s_1 \\ s_2 \end{pmatrix} = \begin{pmatrix} 1 \\ \cos 2\eta \cos 2\theta \\ \cos 2\eta \sin 2\theta \end{pmatrix}, \quad (2)$$

where intensity is normalized as $s_0 = 1$, θ is the rotation angle of the polarization plane and η is the ellipticity. Consequently, the rotation angle θ can be written by

$$\theta = \frac{1}{2}\tan^{-1}\left(\frac{s_2}{s_1}\right). \quad (3)$$

In MO imaging, since the rotation angle due to the MO effect is measured, it is necessary to adjust the origin of the polarization, $\theta = 0°$, corresponding to the absence of an applied magnetic field, which could be obtained by subtracting a background image from a measured image. In addition, the rotation angle measurement using the polarization camera has a disadvantage that it analyzes one polarization from four adjacent pixels, which may result in deterioration of the spatial resolution. For this problem, the pixel interpolation method using Fourier analysis has been proposed [19].

2.2 Transformation of magnetic field

Fig. 1 shows a schematic drawing of calculation model for the MO imaging. The magnetic field $\boldsymbol{H}(\boldsymbol{r})$ at the measurement point $\boldsymbol{r}\,(=(x,y,z))$ in the MO imaging plate is given by the convolution integral of the magnetic pole $\rho(\boldsymbol{r}')$ at the certain place $\boldsymbol{r}'(=(x',y',z'))$ on the sample surface and the transfer function $\boldsymbol{G_H}$, which is given by

$$\boldsymbol{H}(\boldsymbol{r}) = \int_{r'} \rho(\boldsymbol{r}')\,\boldsymbol{G_H}(\boldsymbol{r}-\boldsymbol{r}')d\boldsymbol{r}', \quad (4)$$

where $\boldsymbol{G_H}(\boldsymbol{r})$ is given from Coulomb's law for magnetism [20] as

$$\boldsymbol{G_H}(\boldsymbol{r}) = \frac{\boldsymbol{r}}{4\pi\mu_0|\boldsymbol{r}|^3}. \quad (5)$$

In the frequency domain, the convolution integral in Eq. (5) is given in the form of multiplication according to the convolution theorem as

$$\boldsymbol{H}(k_x,k_y,z) = \rho(k_x,k_y,z')\boldsymbol{G_H}(k_x,k_y,z-z'), \quad (6)$$

where $\boldsymbol{H}(k_x,k_y,z)$ and $\boldsymbol{G_H}(k_x,k_y,z)$ are the Fourier transforms of the magnetic field distribution and the transfer function. Consequently, the Fourier transforms of x-component of the magnetic field distribution $H_x(\boldsymbol{r})$ and y-component of the magnetic field distribution $H_y(\boldsymbol{r})$ can be deduced from z-component of the magnetic field distribution $H_z(\boldsymbol{r})$ and the transfer functions as

$$H_x(k_x,k_y,z) = \frac{G_{Hx}\left(k_x,k_y,z-z'\right)}{G_{Hz}\left(k_x,k_y,z-z'\right)}H_z(k_x,k_y,z) = \mathrm{T}[H_z \to H_x]H_z(k_x,k_y,z) \quad (7)$$

and

$$H_y(k_x,k_y,z) = \frac{G_{Hy}\left(k_x,k_y,z-z'\right)}{G_{Hz}\left(k_x,k_y,z-z'\right)}H_z(k_x,k_y,z) = \mathrm{T}[H_z \to H_y]H_z(k_x,k_y,z), \quad (8)$$

where components of $\boldsymbol{G_H}(k_x,k_y,z)$ are given by

$$G_{Hx}(k_x,k_y,z) = \frac{-ik_x}{2\mu_0\sqrt{{k_x}^2+{k_y}^2}}\exp\left(-\sqrt{{k_x}^2+{k_y}^2}z\right), \quad (9)$$

$$G_{Hy}(k_x,k_y,z) = \frac{-ik_y}{2\mu_0\sqrt{{k_x}^2+{k_y}^2}}\exp\left(-\sqrt{{k_x}^2+{k_y}^2}z\right), \quad (10)$$

$$G_{Hz}(k_x,k_y,z) = \frac{1}{2\mu_0}\exp\left(-\sqrt{{k_x}^2+{k_y}^2}z\right). \quad (11)$$

Consequently, the transformation filters, $\mathrm{T}[H_z \to H_x]$ and $\mathrm{T}[H_z \to H_y]$, are given by

$$\mathrm{T}[H_z \to H_x] = \frac{-ik_x}{\sqrt{{k_x}^2+{k_y}^2}}, \quad (12)$$

and

$$\mathrm{T}[H_z \to H_y] = \frac{-ik_y}{\sqrt{{k_x}^2+{k_y}^2}}. \quad (13)$$

Finally, $H_x(\boldsymbol{r})$ and $H_y(\boldsymbol{r})$ are obtained by as the inverse Fourie transforms of $H_x(k_x,k_y,z)$ and $H_y(k_x,k_y,z)$, respectively.

Furthermore, the signal transformation based on the transfer function can be used to calculate $H_z(x,y,z+\Delta z)$ at a position that is increased by a certain distance Δz from the measured $H_z(x,y,z)$. In this case, the transformation filter $\mathrm{T}[H_z, z \to z+\Delta z]$ becomes

$$\mathrm{T}[H_z, z \to z+\Delta z] = \exp\left(-\sqrt{{k_x}^2+{k_y}^2}\Delta z\right). \quad (14)$$

By combining the distance transformation method with the x- and y-components calculation method, it is possible to obtain the three dimensional (3D) magnetic field distribution from the one-shot measurement.

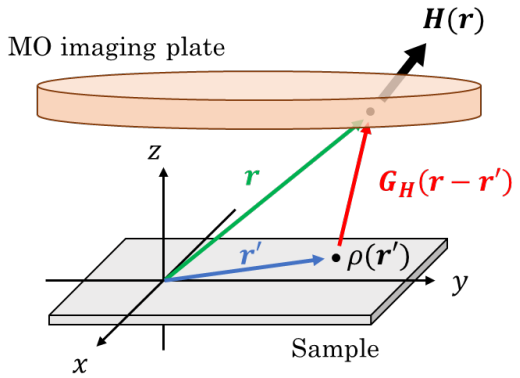

Fig. 1 Schematic drawing of calculation model for MO imaging.

3. Experimental

3.1 MO imaging system using the polarization camera

Fig. 2 shows a schematic drawing of the MO imaging system used in this study. A red LED panel (MISUMI, LEDXR120) with a central wavelength of 630 nm was used as a light source. The linearly-polarized light obtained by a polarizer put on the LED panel vertically illuminated the MO imaging plate. The reflected light

was reflected by a half mirror and captured by a polarization camera (Baumer, VCXU-50MP) having a CMOS with 2448 × 2048 pixels. Image data were imported to a computer via USB connection and were processed by a program written in Python. For the MO imaging plate, Bi-substituted iron garnet films $Nd_{0.5}Bi_{2.5}Fe_5O_{12}$, with a thickness of 600 nm were prepared by a metal-organic decomposition (MOD) method on a glass substrate (Eagle XG, CORNING). Details of the garnet films were described in Ref.14,15,21,22. A 150 nm-thick silver layer was deposited by the sputtering method on the garnet films as a reflective film. The Kerr rotation hysteresis measured by applying a magnetic field in the perpendicular direction to the plane of the MO imaging plate is shown in Fig. 3. Here, the Kerr rotation is equivalent to the Faraday rotation of the garnet film, since the light goes through the garnet film and come back after being reflected by the reflective film. The shape of the hysteresis shows that the rotation angle varies continuously with the perpendicular magnetic field, indicating the easy axis of magnetization is in the in-plane direction. The calibration from the Kerr rotation angle to the magnetic field was done using a linear approximation formula obtained within the range of magnetic saturation. Measurement errors caused by coercivity could solve by using $Gd_3Ga_5O_{12}$ (GGG) substrates, which exhibit small coercivity [23]. Four rectangular-shaped ferrite magnets with a size of 10 mm × 30 mm × 5 mm were used as a sample. The distance Δz from the MO imaging plate was varied from 0 mm to 10 mm.

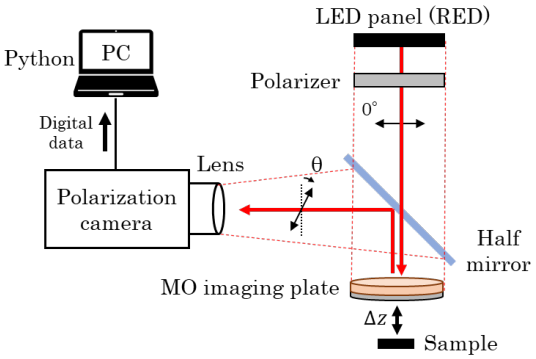

Fig. 2 Schematic diagram of MO imaging system using polarization camera.

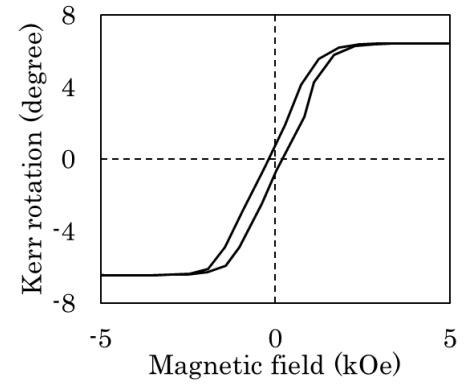

Fig. 3 Kerr rotation hysteresis of MO imaging plate.

3.2 MO imaging of ferrite magnets

Fig. 4 shows a photo of ferrite magnets, $H_z(x,y,0)$ measured by the one-shot measurement with an exposure time of 10 msec, and $H_x(x,y,0)$ and $H_y(x,y,0)$ calculated by the process described in Sec. 2. The 3D magnetic field vectors plotted using $H_z(x,y,\Delta z)$ measured at $\Delta z = 0, 3, 6$ mm and calculated $H_x(x,y,\Delta z)$ and $H_y(x,y,\Delta z)$ are shown in Fig. 5. The magnetic poles of the magnets were clearly observed in $H_z(x,y,0)$, and it was confirmed that sufficient contrast could be obtained even with the one-shot measurement. The values of $H_z(x,y,0)$ consistent with that measured on the sample surface using a Gauss meter. $H_x(x,y,0)$ showed a strong contrast at the boundaries and left and right edges of the magnetic poles, and a weak contrast at the center of each

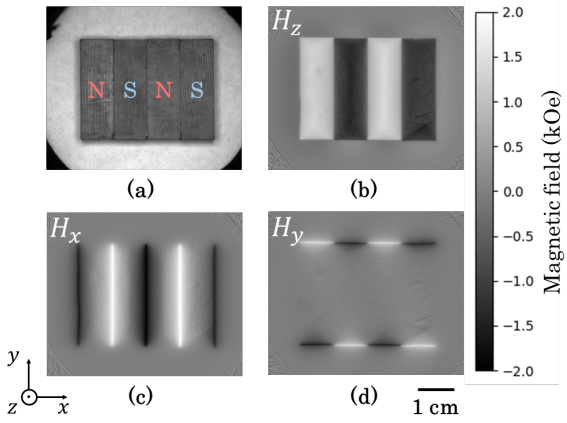

Fig. 4 (a) Digital photograph and magnetic field images, (b) measured $H_z(x,y,0)$, and calculated (c) $H_x(x,y,0)$ and (d) $H_y(x,y,0)$.

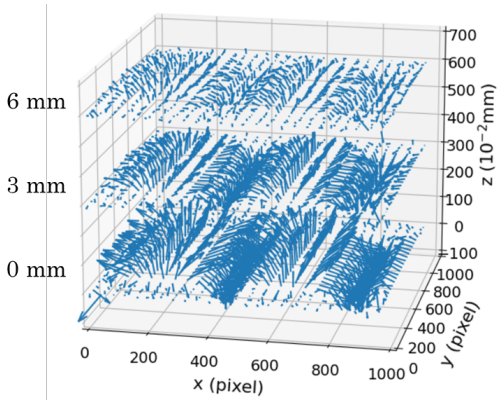

Fig. 5 3D magnetic field vectors above four ferrite magnets measured by MO imaging.

magnet. This result is consistent that the magnetic flux travels from the N-pole to the S-pole. $H_y(x,y,0)$ showed a strong contrast at the top and bottom edges of the magnet and a weak contrast at the center, which is consistent with the behavior of the magnetic flux. These features are consistent with a result of a simulation using Femtet (Murata Software Co., Ltd.), which it is not shown here.

Next, we describe the results of $H_z(x,y,\Delta z)$ calculated from $H_z(x,y,0)$ shown in Fig. 4(b). $H_z(x,y,\Delta z)$ calculated at $\Delta z = 1, 5, 10$ mm are shown in the lower part of Fig. 6(a), and those of actually measured images at $\Delta z = 1, 5, 10$ mm are shown in the upper part for comparison. The line profiles were measured along the center of the magnets as shown with a dotted line in Fig. 6(a). In the actual measurement, the intensity decreases and becomes gradually blurred as the height is increased. The same trend was confirmed in the results of the signal transformation. From the results of the line profile comparison, it was found that the calculated values of the magnetic fields were in good agreement with the measured values except in the vicinity of the peaks. For the height of 1 mm, the calculated data was 18% lower than the measured data, and for the height of 10 mm, the calculated data was 11% higher than the measured data. The difference between the measured and calculated data may be due to the fact that the image contains unnecessary information at the edge of the plate and outside of the MO imaging plate, that is not related to the magnetic field distributions, or that the sample size is too large as compared to the size of the image, resulting in lack of information in the Fourier transforms.

3.3 MO imaging of the electrical steel sheet

We have reported MO imaging over a wide area of a few centimeters, on the other hand, the spatial resolution of MO imaging can reach 0.3 μm, indicating the microscopic scale observations are also possible. The MO imaging plate was placed on a 0.2 mm-thick unpolished electrical steel sheet, and MO imaging was performed with a magnetic field of 465 Oe applied along in-plane direction. Fig. 7 shows an optical image of the sample surface, measured $H_z(x,y,0)$ and calculated $H_x(x,y,0)$, $H_y(x,y,0)$ and azimuth angle $\phi(x,y,0)$ of magnetic field vector. From $H_z(x,y,0)$, strayed magnetic fields from grain boundaries were clearly observed, and stripe magnetic domains were also confirmed. The strayed magnetic field from the grain boundary and the stripe magnetic domain were also observed in the calculated in-plane components. Coarse surface observed in the entire image is thought to be caused by the grain structure of the garnet. It should be noted that longitudinal Kerr microscopy, which is commonly used to observe magnetic domains, requires mirror like surfaces obtained by surface treatments such as polishing, on the other hand, the MO imaging using MO imaging plate has capabilities for visualizing magnetic domain structures without surface treatment.

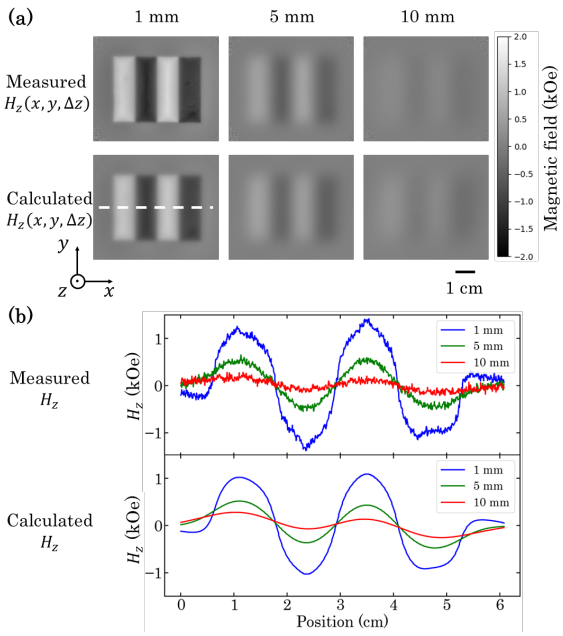

Fig. 6 (a) Measured $H_z(x,y,\Delta z)$ at $\Delta z = 1, 5, 10$ mm and calculated $H_z(x,y,\Delta z)$, (b) line profile along dotted line.

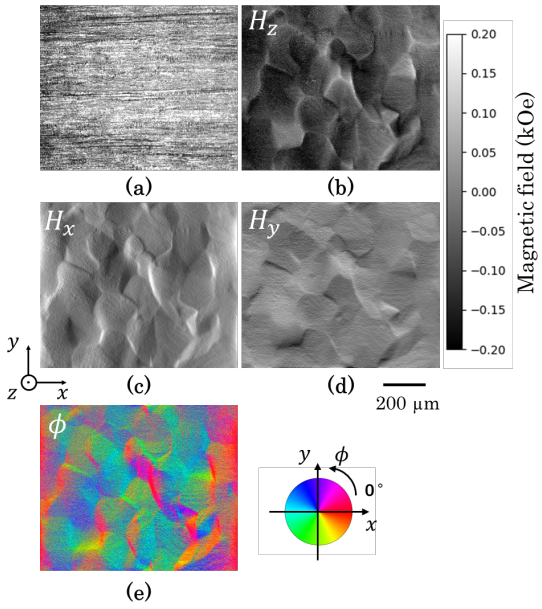

Fig. 7 (a) Optical image of untreated electrical steel sheet and magnetic field images, (b) measured $H_z(x,y,0)$ and calculated (c) $H_x(x,y,0)$, (d) $H_y(x,y,0)$ and (e) azimuth angle $\phi(x,y,0)$.

4. Conclusion

The 3D magnetic field vectors measurements in a 75 mm diameter area with the one-shot measurement by MO imaging using the polarization camera was demonstrated.

The in-plane components, $H_x(\boldsymbol{r})$ and $H_y(\boldsymbol{r})$, were calculated using the signal transformation based on the

transfer function from measured $H_z(\boldsymbol{r})$ by the MO imaging. It was also shown that $H_z(x, y, \Delta z)$ were obtained from measured $H_z(x, y, 0)$. We conclude that this MO imaging technique combined with the signal transformation technique could be a powerful tool for measuring 3D magnetic field vectors in a short time with high accuracy.

Acknowledgements The author thanks Mr. Takashi Yamaguchi of YAMAGUCHI MFG Co., Ltd. for providing the electrical steel sheet. This research was supported in part by JSPS KAKENHI (JP18H03776), the Nanotechnology Platform Program (Molecule and Material Synthesis) of the Ministry of Education, Culture, Sports, Science and Technology (MEXT), Japan, and a joint research program with the Institute of Materials and Systems for Sustainability, Nagoya University.

References

1) S. Gotoh, N. Koshizuka, M. Yoshida, M. Murakami, and S. Tanaka: *J. Appl. Phys.*, **29** 1083 (1990).
2) M. V. Indenbom, N. N. Kolesnikov, M. P. Kulakov, I. G. Naumenko, V. I. Nikitenko, A. A. Polyanskii, N. F. Vershinin, and V. K. Vlasko-Vlasov: *Physica C*, **166** 486 (1990).
3) T. H. Johansen, M. Baziljevich, H. Bratsberg, Y. Galperin, P. E. Lindelof, Y. Shen, and P. Vase: *Phys. Rev. B,* **54,** 16264 (1996).
4) Ch. Jooss, A. Forkl, R. Wrthmann, H.-U. Hbermeier, B. Leibold, and H. Kronmüller: *Physica C*, **266**, 235(1996).
5) Ch. Jooss, J. Albrecht, H. Kuhn, S. Leonhardt, and H. Kronmüller: *Rep. Prog. Phys.,* **65**, 651(2002).
6) T. Ishibashi, Z. Kuang, S. Yufune, T. Kawata, M. Oda, T. Tani, Y. Iimura, and K. Sato: *J. Appl. Phys.*, **100**, 093903 (2006).
7) H. Lee, T. Kim, S. Kim, Y. Yoon, S. Kim, A. Babajanyan, T. Ishibashi, B. Friedman, and K. Lee: *J. Magn. Magn. Mater.,* **322**, 2722 (2010).
8) T. Ishibashi, G. Lou, A. Meguro, T. Hashinaka, M. Sasaki, and T. Nishi: *Sensors and Materials*, **27**, 965 (2015).
9) W. C. Patterson, N. Garraud, E. E. Shorman, and D. P. Arnold: *Rev. Sci. Instrum.*, **86**, 094704 (2015).
10) Y. Nagakubo, Y. Baba, Q. Liu, G. Lou, and T. Ishibashi, *J. Magn. Soc. Jpn.,* **41**, 29 (2017).
11) T. Ishibashi: *J. Magn. Soc. Jpn.,* **44**, 108 (2020).
12) P. E. Goa, H. Hauglin, Å. A. F. Olsen, M. Baziljevich and T. H. Johansen: *Rev. Sci. Instr.,* **74,** 141 (2003) .
13) S. W. Clark and D. Stevens: *IEEE Trans. Ind. Appl.,* **52**, 1469 (2016).
14) T. Yoshida, K. Oishi, T. Nishi, and T. Ishibashi: *European Phys. J. Web of Conf.*, **75**, 05009 (2014).
15) G. Lou, T. Yoshida, and T. Ishibashi: *J. Appl. Phys.*, **117**, 17A749 (2015).
16) G. Lou, T. Kato, S. Iwata, and T. Ishibashi: *Opt. Mater. Express,* **7**, 2248 (2017).
17) Y. Nagakubo, M. Sasaki, S. Meguro, M. Nishikawa, and T. Ishibashi: *J. Appl. Phys.,* **57**, 09TC02 (2018).
18) Y. Maruyama, T. Terada, T. Yamazaki, Y. Uesaka, M. Nakamura, Y. Matoba, K. Komori, Y. Ohba, S. Arakawa, Y. Hirasawa, Y. Kondo, J. Murayama, K. Akiyama, Y. Oike, S. Sato, and T. Ezaki: *IEEE Trans. Elect. Devices*, **65**, 6 (2018).
19) J. S. Tyo, C. F. LaCasse, and B. M. Ratliff: *Opt. Lett.*, **34**, 20 (2009).
20) H. Saito, J. Chen, S. Ishio: *J. Magn. Magn. Mater.,* **191**, 153 (1999).
21) T. Ishibashi, T. Kawata, T. H. Johansen, J. He, N. Harada, and K. Sato: *J. Magn. Soc. Jpn.*, **32**, 150 (2008).
22) T. Ishibashi, A. Mizusawa, M. Nagai, S. Shimizu, and K. Sato: *J. Appl. Phys.,* **97**, 013516 (2005).
23) M. Sasaki, G. Lou, Q. Lin, M, Ninomiya, T. Kato, S. Iwata, and T. Ishibashi: *J. Appl. Phys.,* **55**, 055501 (2016).

Received Nov. 4, 2021; Revised Dec. 27, 2021; Accepted Jan. 15, 2022

J. Magn. Soc. Jpn., **46**, 42-48 (2022)

<Paper>

AC magnetic susceptibility of magnetic nanoparticles measured under DC bias magnetic field

Shoya Noguchi[1], Suko Bagus Trisnanto[1], Tsutomu Yamada[1], Satoshi Ota[2], Yasushi Takemura[1]

[1]Division of Electrical and Computer Engineering, Yokohama National University, *Yokohama 240-8501, Japan*
[2]Department of Electrical and Electronic Engineering, Shizuoka University, *Hamamatsu 432-8561, Japan*

The magnetization dynamics of magnetic nanoparticles are essential for the medical applications of hyperthermia and magnetic particle imaging. In this paper, we clarified the AC magnetic susceptibility of superparamagnetic nanoparticles and their frequency dependence. We measured the AC magnetic susceptibility under an applied DC bias magnetic field. The frequency dependence of AC magnetic susceptibility was clearly observed. The experimentally obtained characteristics of the samples with different effective core diameters and dependence on the intensity of the DC bias magnetic field agreed with the theory assuming a simple particle model. The sample comprising effective core diameters with a wide distribution exhibited different characteristics than the samples comprising magnetically fractionated nanoparticles with a narrower core diameter distribution.

Key words: magnetic nanoparticles, superparamagnetic nanoparticles, AC magnetic susceptibility, magnetization relaxation, Brownian relaxation.

1. Introduction

Magnetic nanoparticles are used in various medical applications, such as magnetic hyperthermia and magnetic particle imaging[1)-3)]. Hyperthermia is a thermal therapy for cancer that uses magnetic nanoparticles as heating agents. The magnetic nanoparticles were heated under an applied AC magnetic field. An AC magnetic field is also applied in magnetic particle imaging. The oscillation of the magnetization of the magnetic nanoparticles is detected from outside the human body. To realize these applications for clinical use, clarifying the excitation conditions of the applied AC magnetic field and the optimum structures of the magnetic nanoparticles is necessary[4)-7)]. Various studies have been conducted to obtain high heat generation from the magnetic nanoparticles and sensitive detection of magnetic nanoparticles, and elucidating the magnetization dynamics of the magnetic nanoparticles is essential[8),9)].

Furthermore, theranostics, which is a concept of combined therapy and diagnosis, has been attracting attention[10),11)]. For example, a simultaneous diagnosis using magnetic particle imaging and hyperthermia using the magnetic nanoparticles has been proposed[11),12)]. As a DC magnetic field of relatively large intensity is applied in magnetic particle imaging as well as magnetic resonance imaging where the magnetic nanoparticles are used as the contrast agent, the magnetization characteristics and heat generation of magnetic nanoparticles under an applied DC bias magnetic field have also been reported[13)-15)].

AC magnetic susceptibility is one of the significant indices representing the AC magnetization characteristics of magnetic materials. The heat generation of the magnetic nanoparticles exhibiting superparamagnetism originates from the delay in the relaxation of the magnetic moment with respect to the applied AC magnetic field[5),16)]. Therefore, the imaginary part of the AC magnetic susceptibility, which reflects the phase delay, is closely related to heat generation. The frequency dependence of the heat generation and AC magnetic susceptibility are essential in terms of magnetization relaxation[17),18)].

The magnetization easy axes and the alignment of magnetic nanoparticles are significant issues in the applications of hyperthermia and magnetic particle imaging. High heat generation and large rotation of magnetization of magnetic nanoparticles are obtained by aligning and fixing the easy axis of magnetization[19),20)]. The harmonic magnetization signal in magnetic particle imaging is influenced by the direction of AC field and DC bias field compared to the direction of the signal detection[21)]. Understanding the magnetization dynamics of magnetic nanoparticles, especially from the quantitative viewpoint, by AC magnetic susceptibility under the DC bias field is critical for their biomedical applications. We reported the heat dissipation of solid-state magnetic nanoparticle samples with their aligned easy axes fixed by a DC magnetic field[18),19)]. In this work, the AC magnetic susceptibility of magnetic fluid nanoparticles under an applied DC bias field was studied. A similar experiment using magnetic nanoparticles from a single core was reported as well[22)]. The multi-core magnetic nanoparticles widely used for biomedical applications[23),24)] were used as samples in this work. We analyzed the magnetization dynamics and Brownian relaxation time derived from the measurements. This study aims to elucidate the magnetic relaxation of magnetic nanoparticles under an applied DC bias field, particularly the imaginary part of AC magnetic

Corresponding author:
Y. Takemura (e-mail: takemura-yasushi-nx@ynu.ac.jp).

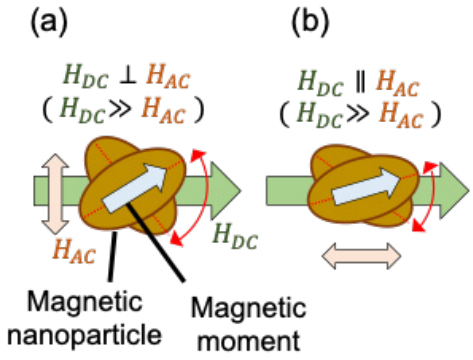

Fig. 1 Magnetization rotation of magnetic nanoparticle under an applied AC magnetic, H_{AC} field with a DC bias magnetic field, H_{DC}. (a) $H_{AC} \perp H_{DC}$, (b) $H_{AC} \parallel H_{DC}$.

susceptibility, which is a key parameter in the medical applications of magnetic nanoparticles.

2. Theory

The magnetization process of a magnetic particle with a single magnetic domain structure is described by the Stoner–Wohlfarth model[25]. As the magnetization of the particle stabilizes its magnetic internal energy, the particle exhibits magnetic anisotropy that aligns the magnetic moment in the stable direction of the energy. This stable direction is called the easy axis of the magnetization. The anisotropy energy, E_a, is described as

$$E_a = K_u V_M \sin^2\theta \tag{1}$$

where K_u, V_M, and θ denote the anisotropy constant, volume of the particle, and angle between the easy axis of magnetization and the magnetic moment, respectively. The Zeeman energy E_H of the magnetic particle under an applied magnetic field H is described as

$$E_H = -mH\cos(\phi - \theta) \tag{2}$$

Here, m and ϕ are the magnetic moment of the particle and the angle between the easy axis and the direction of the applied field H, respectively. The total potential energy of particle E is derived as a summation of the anisotropy energy $E_a$and and Zeeman energy E_H.

$$E = K_u V_M \sin^2\theta - mH\cos(\phi - \theta) \tag{3}$$

The magnetization process of the magnetic particle was determined to minimize the potential energy E.

Magnetic nanoparticles of small volume exhibit a superparamagnetic feature when the effect of thermal fluctuation is not negligible on the anisotropy energy. The magnetization process of the magnetic nanoparticles exhibiting superparamagnetism follows the Langevin function:

$$L(\xi) = \coth(\xi) - \frac{1}{\xi} \tag{4}$$

Here, $\xi = \mu_0 mH/k_B T$, where μ_0, k_B, and T are the magnetic permeability of vacuum, Boltzmann constant, and absolute temperature, respectively.

There are two processes of magnetization relaxation of magnetic nanoparticles: Brownian relaxation and Néel relaxation. The relaxation times τ_B and τ_N are given by

$$\tau_B = \frac{3\eta V_H}{k_B T} \tag{5}$$

$$\tau_N = \tau_0 \exp\left(\frac{K_u V_M}{k_B T}\right) \tag{6}$$

where η is the dynamic viscosity of the fluid, V_H is the hydrodynamic volume, τ_0 is the attempt time, K_u is the magnetic anisotropy constant, and V_M is the volume of the primary particle. These relaxation time equations do not consider the intensity of the applied magnetic field. Two relaxation processes occur simultaneously, and the effective relaxation time is defined as[16]

$$\frac{1}{\tau_{eff}} = \frac{1}{\tau_N} + \frac{1}{\tau_B} \tag{7}$$

A faster relaxation process dominated the effective relaxation time[16]. Recently, we observed the two-step magnetization processes of Brownian and Néel relaxations under applied AC magnetic field[26] and pulse magnetic field[27),28]. Brownian relaxation occurred after Néel relaxation in the magnetic nanoparticle samples exhibiting $\tau_B > \tau_N$ in these experiments. The effects of the oscillation and orientation of the easy axis on the magnetization were also experimentally observed[29].

If the intensity of the applied AC magnetic field is small ($\xi << 1$), the real and imaginary parts of the AC magnetic susceptibility are given by the following equations based on the Debye model, respectively:

$$\chi'(\omega) = \frac{\chi_0}{1+(\omega\tau_{eff})^2} \tag{8}$$

$$\chi''(\omega) = \chi_0 \frac{\omega\tau_{eff}}{1+(\omega\tau_{eff})^2} \tag{9}$$

Here, χ_0 and ω are the susceptibility under an applied magnetic field of low intensity and angular frequency of the AC field, respectively. As $\chi''(\omega)$ of Eq. (9) becomes maximum in the case of $\omega\tau_{eff} = 1$, the effective relaxation time can be derived from the frequency dependence of the real and imaginary parts of the AC magnetic susceptibility.

The Brownian relaxation time of the magnetic particles depends on the intensity of the applied magnetic field[22]. Theoretical analysis of the relaxation time under the applied DC bias magnetic field either perpendicularly (Fig. 1(a)) or parallel (Fig. 1(b)) to an AC magnetic field of low intensity has been reported[30),31]. The Brownian relaxation times of τ_{per} and τ_{para} are given by the following equations:

$$\tau_{per} = \frac{2L(\xi)}{\xi - L(\xi)}\tau_B \tag{10}$$

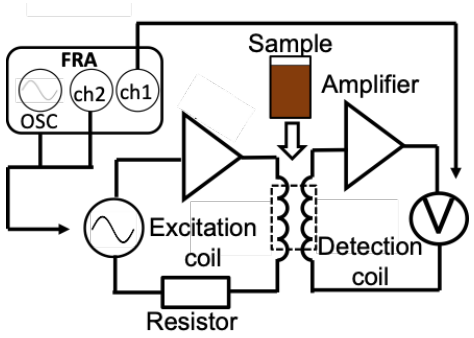

Fig. 2 Circuit diagram of measurement system for AC magnetic susceptibility.

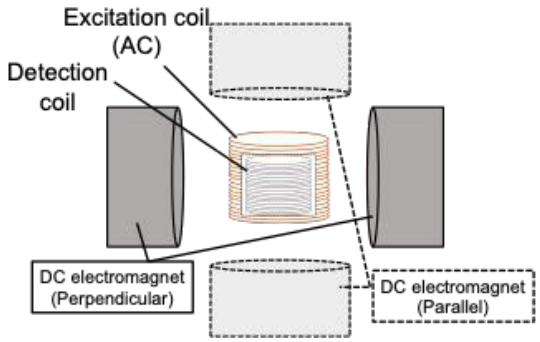

Fig. 3 Configuration of AC excitation field coil, DC bias field coil and detection coil.

$$\tau_{para} = \frac{dlnL(\xi)}{dln\xi}\tau_B \tag{11}$$

Here, $\xi = \mu_0 mH/k_B T$ is proportional to H, and H is the intensity of the applied DC field in these equations. The intensity of the DC field is assumed to be larger than that of the AC field.

3. Experiments

3.1 Measurement samples

Three fluid samples containing magnetic nanoparticles were used in this study. The first sample was Resovist®, which is a commercially distributed contrast agent for the clinical diagnosis of magnetic resonance imaging. It is a water-based colloidal solution of γ-Fe_2O_3/Fe_3O_4 coated with carboxydextran. The effective core diameter was 6–21 nm[24].

The second and third samples were prepared through magnetic separation of Ferucarbotran, which is the raw material for Resovist®. These samples were supplied by Meito Sangyo Co., Ltd., Japan. The structural and magnetic properties of magnetically fractionated nanoparticles from Ferucarbotran were reported by Yoshida et al[24),32]. They denoted the samples as MS1, MS2, and MS3, whose effective core diameters were 21.6, 10.7, and 6.2 nm, respectively. In this study, MS1 and MS2 were used.

The density and volume of the three samples were 28 mgFe/ml and 100 µl, respectively.

3.2 Measurement method

A DC magnetization curve of the samples was measured using a vibrating sample magnetometer (VSM, VSM-3, Toei Industry Co., Ltd., Tokyo, Japan) at room temperature. The maximum intensity of the applied magnetic field was $\mu_0 H = 1.5$ T.

The AC magnetic susceptibility was measured using a frequency response analyzer (FRA, FRA51615, NF Corporation, Yokohama, Japan). The intensity and frequency range of the applied AC magnetic field were $\mu_0 H = 0.09$ mT and 100 Hz–1 MHz, respectively. Figure 1 shows the measurement circuit system used in this study[33]. In this measurement, the detection coil was aligned concentrically to the excitation coil. The excitation AC magnetic field, $H(t) = H_0 \cos\omega t$, was applied to the sample using the oscillator of the FRA. Here, H_0 denotes the amplitude of the AC field.

The voltage V_0 induced in the detection coil without an inserted sample is described as

$$V_0(t) = NS\omega\mu_0 H_0 \sin\omega t \tag{12}$$

where N and S are the number of turns and the cross-sectional area of the detection coil, respectively. When the sample is inserted in the detection coil, the induced voltage V_s is changed to

$$V_s(t) = NS\omega\mu_r\mu_0 H_0 \sin(\omega t - \beta) \tag{13}$$

where μ_r and β are the amplitude ratio and phase delay of the induced voltage with and without a sample, respectively. These are essential parameters in AC magnetic permeability and susceptibility. The complex magnetic permeability $\boldsymbol{\mu_r}$ is described using μ_r and β as follows:

$$\boldsymbol{\mu_r} = \mu_r(cos\beta - jsin\beta) \tag{14}$$

A complex magnetic susceptibility $\boldsymbol{\chi}$ can be derived from $\boldsymbol{\mu_r}$.

$$\boldsymbol{\mu_r} = 1 + \boldsymbol{\chi} \tag{15}$$

$$= 1 + \chi' - j\chi'' \tag{16}$$

From the above equations, the real and imaginary parts, and the absolute value of the AC magnetic susceptibility are described as

$$\chi' = \mu_r cos\beta - 1 \tag{17}$$

$$\chi'' = \mu_r sin\beta \tag{18}$$

$$|\boldsymbol{\chi}| = \sqrt{\chi'^2 + \chi''^2} \tag{19}$$

respectively. In this study, μ_r and β were derived by measuring the induced voltage in the detection coil, and the AC magnetic susceptibility was calculated using Eqs. (17), (18), and (19).

The AC magnetic susceptibility was measured under an

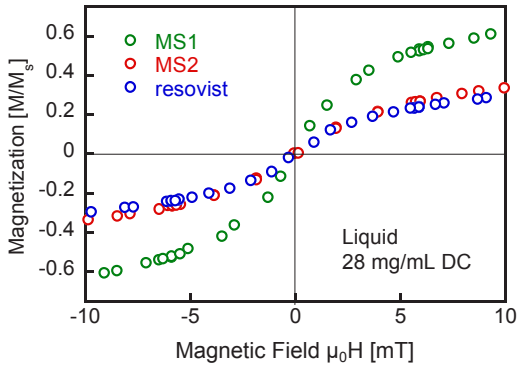

Fig. 4 DC magnetization curves of the samples (parts of major magnetization curves).

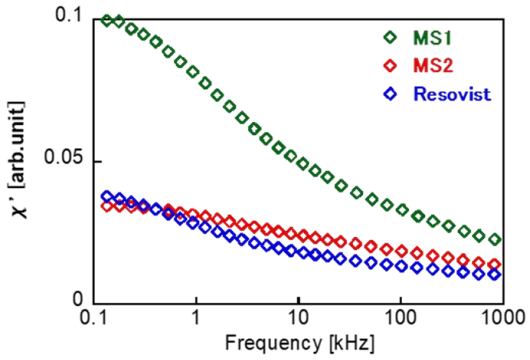

Fig. 5 Real part of AC magnetic susceptibility of the samples.

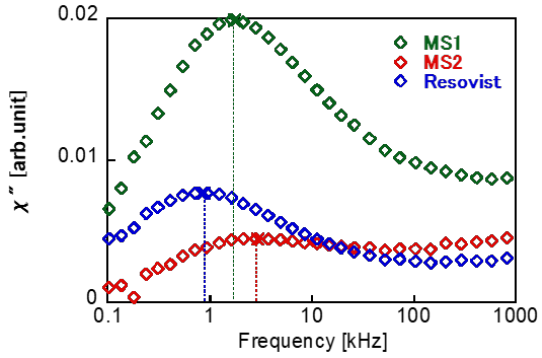

Fig. 6 Imaginary part of AC magnetic susceptibility of the samples.

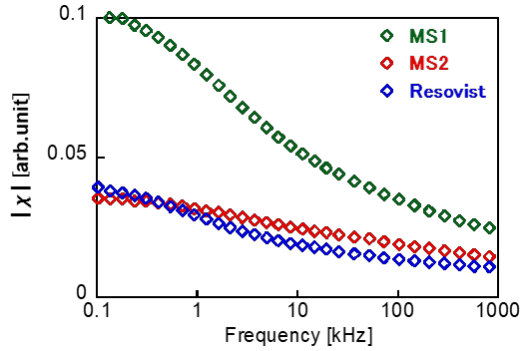

Fig. 7 Absolute value of AC magnetic susceptibility of the samples.

applied DC bias magnetic field. A DC electromagnet was used, as shown in Figure 3. The direction of the DC bias field was either parallel or perpendicular to that of the AC excitation field. The intensity of the DC bias field was $\mu_0 H$ = 0–8 mT.

4. Results and Discussion

4.1 DC magnetization curves

Figure 4 shows the measured DC magnetization curves of the samples. The major magnetization curves were traced under the applied magnetic field of up to $\mu_0 H$ = ±1.5 T. The figure shows the parts of the major curves corresponding to the range between $\mu_0 H$ = ±10 mT. All samples exhibited a superparamagnetic feature with no remanent magnetization[24),32)]. The magnetization of MS1 was greater than that of Resovist and MS2, which was attributed to the larger effective core diameter of MS1. The magnetization curves of Resovist and MS2 were equivalent.

The average values of the magnetic moment, m, were calculated from the DC major magnetization curves using the singular value decomposition method[34),35)]. They were obtained as m = 5.6×10^{-18}, 1.2×10^{-18}, and 1.3×10^{-18} Am² for MS1, MS2, and Resovist at a density of 28 mgFe/ml, respectively. Moreover, m = 2.3×10^{-18} and 5.0×10^{-19} Am² for MS1 and MS2 at a density of 0.67 mgFe/ml, respectively, were reported[32)].

4.2 AC magnetic susceptibility without DC bias field

The real and imaginary parts of the AC magnetic susceptibility of the samples measured without the DC bias field are shown in Figures 5 and 6, respectively. Figure 7 shows the absolute values of the susceptibility. The real part, as well as the absolute value, are reduced as the AC frequency increases. This is because the rotation of the magnetic moment cannot follow the change in the applied magnetic field. The imaginary part is remarkably less than the real part, so the real part is almost equivalent to the absolute value.

The frequency peak, f observed in the imaginary parts shown in Figure 6 is related to the Brownian relaxation time τ_B ($f = 1/2\pi\tau_B$)[26)]. From the figure, the magnitude relationship of τ_B is as follows: Resovist > MS1 > MS2. Because τ_B is described by Eq. (5), it is dependent on the viscosity of the fluid and hydrodynamic diameter of the nanoparticle. Although MS1 consisted of large particles fractionated from Ferucarbotran, the τ_B of Resovist was larger than that of the other two samples.

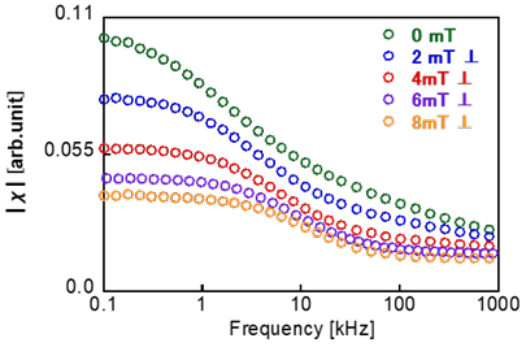

Fig. 8 Absolute value of AC magnetic susceptibility of MS1 ($H_{AC} \perp H_{DC}$).

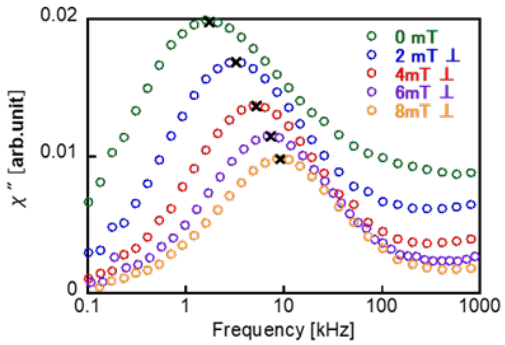

Fig. 9 Imaginary part of AC magnetic susceptibility of MS1 ($H_{AC} \perp H_{DC}$).

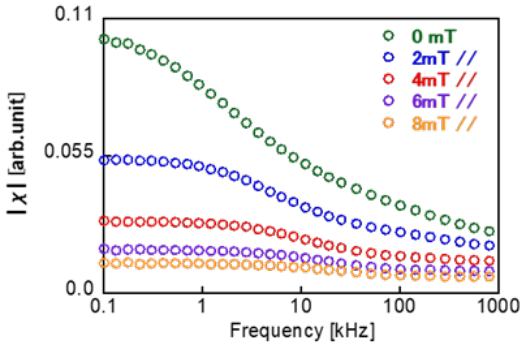

Fig. 10 Absolute value of AC magnetic susceptibility of MS1 ($H_{AC} \parallel H_{DC}$).

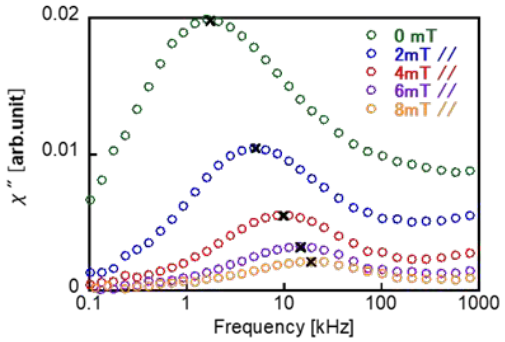

Fig. 11 Imaginary part of AC magnetic susceptibility of MS1 ($H_{AC} \parallel H_{DC}$).

4.3 AC magnetic susceptibility under DC bias field

The absolute value and imaginary part of the AC magnetic susceptibility of MS1 under the DC bias magnetic field applied perpendicular to the AC magnetic field ($H_{AC} \perp H_{DC}$) are shown in Figures 8 and 9, respectively. Figures 10 and 11 show the absolute value and imaginary part under the DC bias magnetic field applied parallel to the AC magnetic field ($H_{AC} \parallel H_{DC}$), respectively.

The peak frequencies of the imaginary parts shown in Figures 9 and 11 increased when the DC bias field was applied whether perpendicular or parallel to the AC field. There was a decrease in τ_B caused by the DC bias field. This originated from the decrease in the oscillating rotation angle of the magnetization which was aligned in a stable state by the DC field. The formation of a chain structure of the magnetic particles under the DC bias field is possible; however, this is difficult to confirm in fluid samples[36]. The absolute values reduced by the DC bias field shown in Figures 8 and 10 were also caused by the decrease in the oscillating rotation angle of the magnetization.

It was also found that this decrease of the absolute values was more pronounced when the DC bias field was applied in the parallel direction than in the perpendicular direction. Here, two physical mechanisms associated with the magnetization of magnetic nanoparticles are suggested. The first mechanism is that the rotation angle of the oscillating magnetization under $H_{AC} \parallel H_{DC}$ is smaller than that under $H_{AC} \perp H_{DC}$. The magnetization oscillated by the applied AC magnetic field below 100 kHz is predominantly caused by particle rotation with the Brownian relaxation[26]. Second, the change in magnetization along the direction of the AC excitation and detection is reduced under $H_{AC} \parallel H_{DC}$. The oscillation angle of the magnetization decreases with increasing DC field intensity. We obtained characteristics equivalent to those of the other two samples of MS2 and Resovist.

4.4 Brownian relaxation time under DC bias field

Figure 12(a) shows the dependences of MS1 and MS2 τ_B on the DC bias field intensity. They are derived from the peak frequencies of the imaginary part of the AC susceptibility. Figures 12(b) and (c) show the τ_B of MS1 and MS2 under $H_{AC} \perp H_{DC}$ and $H_{AC} \parallel H_{DC}$ normalized by those of $H_{DC} = 0$. The theoretical τ_B curves calculated using Eqs. (10) and (11) assuming $T = 300$ K, $m = 5\times10^{-18}$, and 7×10^{-18} Am^2 for MS1 and MS2, respectively, are also shown. They were normalized by τ_B in the case of

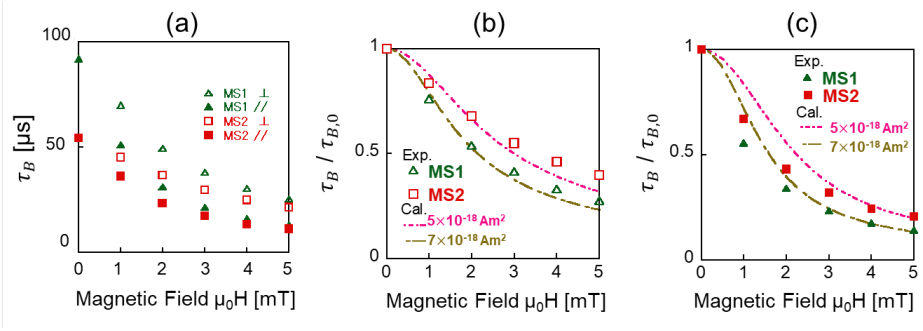

Fig. 12 (a) Dependence of Brownian relaxation time on DC bias field intensity of MS1 and MS2. (b) Brownian relaxation time under $H_{AC} \perp H_{DC}$ normalized by that of H_{DC}=0. (c) Brownian relaxation time under $H_{AC} \parallel H_{DC}$ normalized by that of H_{DC}=0.

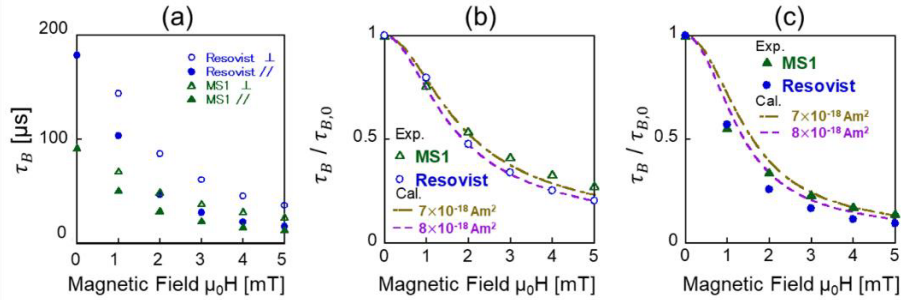

Fig. 13 (a) Dependence of Brownian relaxation time on DC bias field intensity of Resovist and MS1. (b) Brownian relaxation time under $H_{AC} \perp H_{DC}$ normalized by that of H_{DC}=0. (c) Brownian relaxation time under $H_{AC} \parallel H_{DC}$ normalized by that of H_{DC}=0.

$\mu_0 H = 0$ mT in Eqs. (10) and (11). The assumed values of m do not represent those assigned to the samples, instead they were determined to fit the experimentally obtained results. The decrease in τ_B of MS1 with increasing DC bias field intensity is more pronounced than that of MS2, whose characteristic is observed in both cases of $H_{AC} \perp H_{DC}$ and $H_{AC} \parallel H_{DC}$. This significant decrease in τ_B of MS1 is attributed to its larger effective core diameter than that of MS2. These experimental results qualitatively agree with Eqs. (10) and (11). The decrease in τ_B is remarkable for particles with larger m, as shown in Figures 12(b) and (c). The oscillating angle of MS1, which exhibited a larger magnetic moment than MS2, was greatly reduced by applying a DC bias field. The values of $m = 7\times10^{-18}$ and 5×10^{-18} Am^2 for MS1 and MS2, respectively, fit the applied field intensity dependence of the experimentally obtained values of τ_B. However, they were larger than those determined from the DC magnetization measurements ($m = 5.6\times10^{-18}$ and 1.2×10^{-18} Am^2 for MS1 and MS2, respectively). These differences presumably arise from the difference in the range of the applied field intensity: $\mu_0 H = \pm5$ mT for Figures 12(b) and (c), and $\mu_0 H = \pm1.5$ T for the DC magnetization curve.

Figures 13(a), (b), and (c) show the measured results of Resovist and MS1. The calculated curves of τ_B are shown in Figures 13(b) and (c). Considering the preparation method of MS1 and the value of m derived from the DC magnetization curve, MS1 is supposed to exhibit a greater magnetic moment on average and is more effective than Resovist. Nevertheless, the measured results of Resovist and MS1 shown in Figure 13 indicated that the decrease in τ_B of Resovist with increasing DC bias field intensity was more pronounced than that of MS1. From the viewpoint of the magnitude of m, this result does not agree with Eqs. (10) and (11). A simple analysis using Eqs. (10) and (11) that assume a single particle diameter is not possible in this case because of the wide variance of the magnetic moments in Resovist. Its core diameter is distributed in the range of 6–21 nm. Although the theoretical curve of Resovist was quantitatively fitted with the experimental result using $m = 8\times10^{-18}$ Am^2, it is not appropriate to discuss a single value of m for Resovist, which exhibits wide variance in particle diameter.

5. Summary

We measured the AC magnetic susceptibility of the magnetic nanoparticle samples under an applied DC bias field. The samples were MS1, MS2, and Resovist. MS1 and MS2 were magnetically fractionated Ferucarbotran, which is the raw material of Resovist. Resovist exhibited a wide distribution of effective core diameters between 6 and 21 nm. The effective core diameters of MS1 and MS2 were 21.6 nm and 10.7 nm, respectively. The absolute values and real and imaginary parts of the AC magnetic susceptibility of the samples were experimentally determined. We clarified the dependence of these parameters on the AC magnetic susceptibility in the direction of the DC bias field and its intensity. The difference in the AC magnetic susceptibility between MS1 and MS2 supported the theory of relaxation time under the bias field. Nevertheless, we found that the difference between Resovist and MS1 did not agree with the theory, assuming a simple particle model. This was attributed to the wide variance of the magnetic moments in Resovist. It is expected that a further study on the quantitative analysis of AC magnetic susceptibility and its relationship to heat dissipation and harmonic signals will contribute to the biomedical applications of magnetic nanoparticles.

Acknowledgements This work was partially supported by the JSPS KAKENHI 20H05652 and 20H02163.

References

1) Q. A. Pankhurst, N. K. T. Thanh, S. K. Jones, and J. Dobson: *J. Phys. D*, **42**, 224001 (2009).
2) A. Jordan, R. Scholz, P. Wust, H. Fähling, and R. Felix: *J. Magn. Magn. Mat.*, **201**, pp. 413–419 (1999).
3) B. Gleich and J. Weizenecker: *Nature*, **435**, pp. 1214–1217 (2005).
4) A. Tomitaka, R. M. Ferguson, A. P. Khandhar, S. J. Kemp, S. Ota, K. Nakamura, Y. Takemura, and K. M. Krishnan: *IEEE Trans. Magn.*, **51**, 6100504 (2015).
5) H. Mamiya and B. Jeyadevan: *Sci. Rep.*, **1**, 157 (2011).
6) P. Bender, J. Fock, C. Frandsen, M. F. Hansen, C. Balceris,F. Ludwig, O. Posth, E. Wetterskog, L. K. Bogart, P. Southern, W. Szczerba, L. Zeng, K. Witte, C. Gruttner, F. Westphal, D. Honecker, D. GonzalezAlonson, L. F. Barquin, and C. Johansson: *J. Phys. Chem.*, **122**, pp. 3068-3077 (2018).
7) S. Ota, S. B. Trisnanto, S. Takeuchi, J. Wu, Y. Cheng, and Y. Takemura: *J. Magn. Magn. Mater.*, **538**, 168313 (2021).
8) T. Yoshida and K. Enpuku: *J. Appl. Phys.*, **48**, 127002 (2009).
9) S. B. Trisnanto and Y. Kitamoto: *AIP Conf. Proc.*, **1807**, 020021 (2017).
10) K. Hayashi, M. Nakamura, W. Sakamoto, T. Yogo, H. Miki, S. Ozaki, M. Abe, T. Matsumoto, and K. Ishimura: *Theranostics*, **3**, pp. 366–376 (2013).
11) D. Hensley, Z. W. Tay, R. Dhavalikar, B. Zheng, P. Goodwill, C. Rinaldi, S. Conolly: *Phys. Med. Biol.*, **62**, pp. 3483–3500 (2017).
12) Z. W. Tay, P. Chandrasekharan, A. Chiu-Lam, D. W. Hensley, R. Dhavalikar, X. Y. Zhou, E. Y. Yu, P. W. Goodwill, B. Zheng, C. Rinaldi, and S. M. Conolly: *ACS Nano*, **12**, pp. 3699-3713 (2018).
13) R. Onodera, E. Kita, M. Kishimoto, T. Kuraiwa, and H. Ynagihara: *IEEE Trans. Magn.*, **57**, 6100605 (2021).
14) K. C. Ugochukwu, M. M. Sandiq, E. S. Biegel, L. Meagher, M. R. Hill, K. G. Sandeman, A. Haydon, and K. Suzuki: *AIP Adv*, **10**, 015128 (2020).
15) B. Mehdaoui, J. Carrey, A. Cornejo, C. Nayral, F. Delpech, B. Chaudret, and M. Respaud: *Appl. Phys. Lett.*, **100**, 05403 (2012).
16) R. E. Rosensweig: *J. Magn. Magn. Mat.*, **252**, pp. 370-374 (2002).
17) S. Ota, T. Yamada, and Y. Takemura: *J. Appl. Phys.*, **117**, 17D713(2015).
18) T. Ymaminami, S. Ota, S. B. Trisnanto, M. Ishikawa, T. Yamada, T. Yoshida, K. Enpuku, Y. Takemura: *J. Magn. Magn. Mat.*, **517**, 167401 (2021).
19) G. Shi, R. Takeda, S. B. Trisnanto, T. Yamada, S. Ota, and Y. Takemura: *J. Magn. Magn. Mat.*, **473**, pp. 148-154 (2019).
20) A. L. Elrefai, K. Enpuku, and T. Yoshida: *J. Appl. Phys.*, **129**, 093905 (2021).
21) S. Ota, K. Nishimoto, T. Yamada, and Y. Takemura: *AIP Adv.*, **10**, 015007 (2020).
22) J. Dieckhoff, D. Eberbeck, M. Schilling, and F. Ludwig: *J.Appl. Phys.*, **119**, 043903 (2016).
23) R. Ludwig, M. Stapf, S. Dutz, R. Müller, U. Teichgräber, and I. Hilger: *Nanoscale Res. Lett.*, **9**, 602 (2014).
24) T. Yoshida, N. B. Othman, and K. Enpuku: *J. Appl. Phys.*, **114**, 173908 (2013).
25) E. C. Stoner and E. P. Wohlfarth: *Trans. R. Soc. London. Ser. A*, **240**, pp. 599-642 (1948).
26) S. Ota and Y. Takemura: *Appl. Phys. Express.*, **10**, 085001 (2017).
27) S. B. Trisnanto, S. Ota, and Y. Takemura: *Appl. Phys. Express.*, **11,** 075001 (2018).
28) S. Ota and Y. Takemura: *J. Appl. Chem. C*, **123**, pp. 28859-28866 (2019).
29) S. Ota, S. Ohkawara, H. Hirano, M. Futagawa, and Y. Takemura: *J. Magn. Magn. Mat.*, **539**, 168354 (2021).
30) W. T. Coffey, P. J. Cregg, and Yu. P. Kalmykov: *Adv. Chem. Phys.*, **83**, 263 (2007).
31) J. Zhong, N. Luncht, B. Hankiewicz, M. Schilling, and F. Ludwig: *Appl. Phys. Lett.*, **115**, 133102 (2019).
32) T. Sasayama, T. Yoshida, K. Tanabe, N. Tsujimura, and K. Enpuku: *IEEE Trans. Magn.*, **51**, 5101504 (2015).
33) S. B. Trisnanto and Y. Kitamoto: *J. Phys. Chem. C*, **123**, pp. 23732-23737 (2019).
34) T. Sasayama, T. Yoshida, and K. Enpuku: Magnetic Moment Distribution Analysis Software With SVD Method for MNPs. [Online]. Available: http://www.sc.kyushuu.ac.jp/~enlab/sasayama/software.html (As of October 29, 2021).
35) T. Sasayama, T. Yoshida, M. M. Saari, and K. Enpuku: *J. Appl. Phys.*, **117**, 17D155 (2015).
36) E. Myrovali, N. Maniotis, A. Makridis, A. Terzopoulou, V. Ntomprougkidis, K. Simeonidis, D. Sakellari, O. Kalogirou, T. Samaras, R. Salikhov, M. Spasova, M. Farle, U. Wiedwald, and M. Angelakeris: *Sci. Rep.*, **6**, pp. 1-11 (2016).

Received Oct. 07, 2021; Revised Nov. 17, 2021; Accepted Dec. 06, 2021

Journal of the Magnetics Society of Japan

Vol. 46 No. 2 (通巻第320号) 2022年3月1日発行

Vol. 46 No. 2 Published Mar. 1, 2022
by the Magnetics Society of Japan
Tokyo YWCA building Rm207, 1–8–11 Kanda surugadai, Chiyoda-ku, Tokyo 101–0062
Tel. +81–3–5281–0106 Fax. +81–3–5281–0107

Printed by JP Corporation Co., Ltd.
Sports Plaza building 401, 2–4–3, Shinkamata Ota-ku, Tokyo 144–0054
Advertising agency: Kagaku Gijutsu-sha

発行：(公社)日本磁気学会 101–0062 東京都千代田区神田駿河台 1–8–11 東京YWCA会館 207 号室
製作：ジェイピーシー 144–0054 東京都大田区新蒲田 2–4–3 スポーツプラザビル401 Tel.（03）6715–7915
広告取扱い：科学技術社 111–0052 東京都台東区柳橋 2–10–8 武田ビル4F Tel.（03）5809–1132